

**UNIVERSITÀ DEGLI STUDI DI NAPOLI
FEDERICO II**



SCUOLA POLITECNICA E DELLE SCIENZE DI BASE

Dipartimento di Ingegneria chimica, dei Materiali e della Produzione
Industriale

TESI DI LAUREA MAGISTRALE

IN

INGEGNERIA CHIMICA

Investigation on the role of load volume in pyro-electrodynamic jetting

Supervisor

Prof. Pier Luca Maffettone

Candidate

Marilina Mancini

Matricola M55001190

Advisor

Dr. Simonetta Grilli

ANNO ACCADEMICO 2021-2022

Summary

Introduction.....	2
Chapter 1: State of the art.....	5
1.1 The pyroelectric effect.....	5
1.2 Electro-hydrodynamic (EHD) emission.....	9
1.3 EHD printing configurations.....	14
Chapter 2: Materials and methods	20
2.1 Setup description.....	20
2.2 Sample solution and slides.....	28
2.3 Pin-cleaning.....	31
2.4 Spot analysis.....	32
Chapter 3: Results and discussion.....	35
3.1 Spot diameter and intensity at 500 pg/ml.....	36
3.2 Spot diameter and intensity at 0.8 pg/ml.....	46
3.3 Effect of the number of the jets.....	55
3.4 Volume dispensed.....	57
Chapter 4: Conclusions.....	59
4.1 Conclusions and future perspectives.....	59
References.....	61

INTRODUCTION

The thesis work presented is part of two research projects: the first is the **Asi-Unina** project, a project aimed at developing innovative technologies for health in space, while the second is the European **SensApp** project, a project aimed at developing a super sensor capable, through a blood test, of making an early diagnosis of Alzheimer's disease. Thanks to the collaboration between the University of Naples Federico II and the Institute of Applied Sciences and Intelligent Systems of the National Research Council (CNR-ISASI) it was possible to carry out the experimental tests of the thesis at the CNR labs.

The SensApp project (agreement n.829104) is funded by the research and innovation program 'European Union's Horizon 2020' and involves six partners (CNR, Vrije Universiteit Brussel VUB, Johannes Kepler University Linz JKU, Technical Research Centre of Finland VTT, Centro Neurolesi Pulejo Messina, Ginolis GIN).

At the base of the early diagnosis of Alzheimer's disease is the search for biomolecular markers related to the disease (Beta-amyloid, tau, P-tau) in human plasma. There are already techniques capable of carrying out this detection such as the ELISA procedure, an enzyme-linked immunosorbent assays capable of quantifying proteins and qualifying their activation status in complex biological samples [1,2]. This however has important limitations: first of all it has a low sensitivity, in fact it reaches an LOD detection limit of about 50 pg/mL (the level in peripheral blood is less than 1 pg/mL) [3],

secondly it appears to be invasive for the patient as the analysis is performed from cerebrospinal fluid (CSF) samples [3]. The super sensor aims to overcome these limitations with a detection limit falling below 1 pg/mL.

This is possible thanks to the innovative 'pyroelectrodynamic jet' technology, which allows one to obtain, starting from a determined volume of body fluid, small and highly concentrated droplets of biomolecules (e.g. biomarkers) through an electro-hydrodynamic phenomenon. The high-rate of accumulation of these solution droplets on a reaction slide allows one to overcome the LODs provided by standard methods.

The idea was then extended to the diagnosis of various chronic diseases, assessing the concentration of antibodies not only in human plasma but also in other peripheral body fluids such as saliva, tears, urine etc. An example is the search for collagen as a biomarker of chronic diseases [4]. All to build and apply wearable sensors, capable of detecting targets through real-time detection [5-7]. The predominant factor of other body fluids also continues to be the low concentration of analytes with very small volumes available [8].

The contribution of this thesis work is to investigate the role of the loaded solution volume on the behaviour of spot's diameter and spot's fluorescence intensity, representative of the number of biomolecules presents in the loaded solution volume. This was done by fixing the concentration and varying the load volume.

Furthermore, the fluorescence intensity of the spots was investigated at different amounts of jets, to study the effect of the accumulation on the detection level of the molecules.

The thesis is structured as follows:

- state of the art concerning the pyro-electrohydrodynamic effect;
- materials and methods;
- results and discussion;
- conclusions and future perspective.

Chapter 1

STATE OF THE ART

1.1 THE PYROELECTRIC EFFECT

The pyroelectric effect is related to the pyroelectricity of some materials, which consists in the ability of certain materials to accumulate temporary surface charges and voltage as a direct consequence of a heating or cooling treatment [9]. Examples of pyroelectric materials are ferroelectric crystals (such as lithium niobate LiNbO_3 , Barium titanate BaTiO_3 ect), which exhibit spontaneous electrical polarization. In particular, lithium niobate (LN) crystals were used in this thesis work, where the lack of inversion symmetry induces various effects including pyroelectricity [10]. When the ferroelectric crystal is not subjected to any thermal source and is at room temperature, it is in an electrically neutral condition or the spontaneous polarization P_S is completely compensated by the surface shielding charges as shown in the Fig.1 [11].

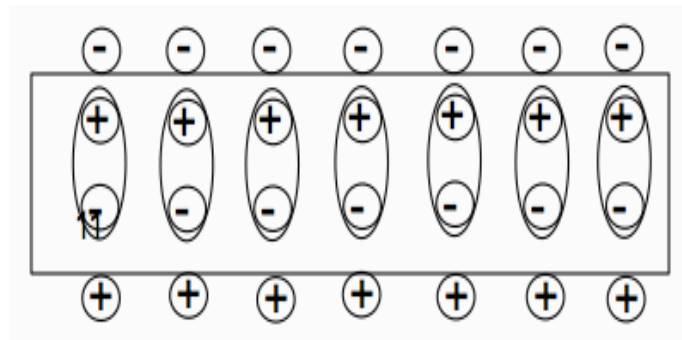


Fig. 1 | Schematic view of the cross section of the ferroelectric crystal with charge distribution shown at equilibrium.

When a heating treatment is applied to the ferroelectric crystal, a modification of the positions of the atoms within the crystalline structure occurs [9] causing an excess of surface charge (Fig.2).

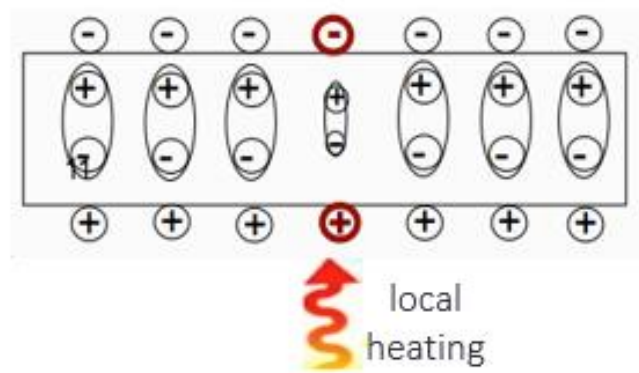


Fig. 2 | Schematic view of the cross section of the ferroelectric crystal with charge distribution shown in the presence of a thermal source.

The heating therefore determines a lack of local compensation between the spontaneous polarization P_S and the surface charges. The polarization variation (ΔP_S) is proportional to the applied temperature gradient (ΔT):

$$\Delta P_S \propto \Delta T$$

and generate a transient state in which the surface shielding charges (shielding) are in excess respect to the polarization charge leading to a relatively high electric field [11].

The thermal stimulation can be applied by different means such as a far infrared laser (e.g., CO₂ laser source), which generates vibrational states associated with the local heating of the crystal [12]; a micro-heater made of a titanium coil integrated on the surface of the crystal, which generates a current with local heating due to the Joule effect [8]; a Peltier cell, which is

a thermoelectric device, where an appropriate voltage generates a heat transfer effect.

The electric field generated in correspondence of the heated part has an intensity that is comparable to that generated by conventional high voltage power supplies [13].

Several studies have been conducted on the influence of temperature's variation and crystal size has on the behaviour of the electric field.

For example, the trend of the temperature inside the ferroelectric crystal has been identified, which appears to be time-dependent (Fig.3) [8].

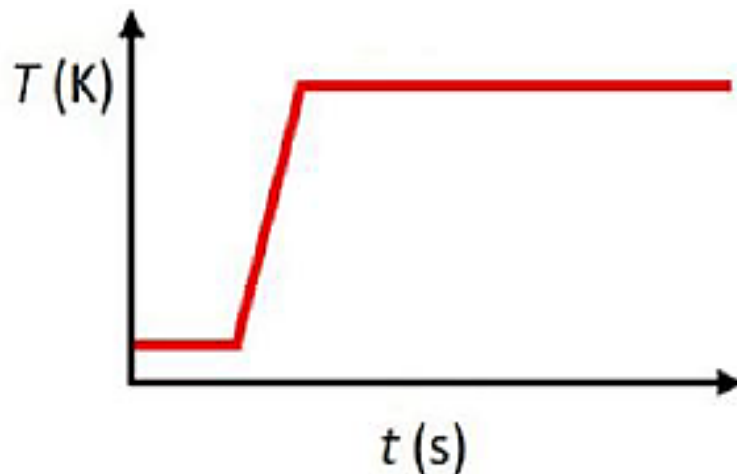


Fig. 3 | The shape of the crystal temperature depends on time.

The results reported [8] show the behaviour of the electric voltage generated on the crystal surface as a response to a linearly rising temperature. The electrical potential increases linearly up to a maximum value and then decays when the temperature is kept constant, as shown in Fig. 4.

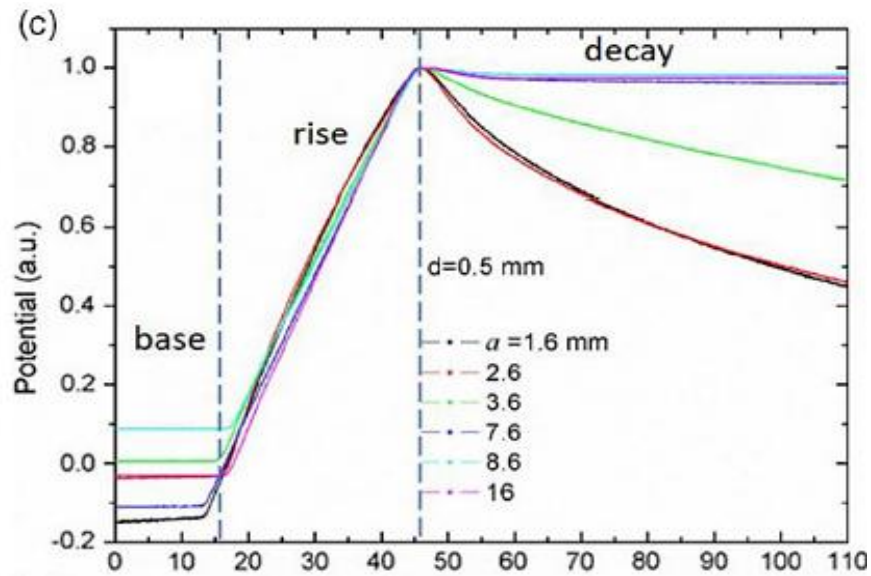


Fig. 4 | Time behaviour of the electrical potential for crystals with a thickness $d=0.5\text{mm}$ and $d=1\text{ mm}$ respectively.

It's believed that the decay of the electric potential is mostly related to the recombination of the charge on the crystal surface and the environmental ions produced by the electrical breakdown along the edges of the crystal, where the breakdown threshold is exceeded [8]. Thicker crystals show faster decay as they create a higher electric field at the edges [8].

The electric field generated by the crystal serves to hit the mother drop of the sample solution which will generate the highly concentrated droplets which will decay with a high speed. The above-mentioned study suggested the most appropriate crystal size for producing a high droplet ejection rate.

Do not exceed the temperature gradient as temperatures that are too high could damage the functional characteristics of the biological liquids to be analysed; the electric field must only be sufficient to activate the jet of liquid. The pyroelectric effect is therefore a way to generate electric fields without the use of electrodes and external circuits.

1.2 ELECTRO-HYDRODYNAMIC (EHD) EMISSION

The electric field obtained by heating the ferroelectric crystal can be used for the ejection of tiny droplets starting from the mother drop of solution.

The electric field produced by the crystal hits the meniscus of the mother drop of liquid pending from a support, which can be a capillary tube, a nozzle or an orifice, and deforms it into the so-called Taylor's cone [8]. The liquid drop is initially stable with interfacial tension and gravity balanced, afterwards, due to the effect of the electric field, a di-polarization is created in the drop or a repulsive force arises between the charges with same sign (Fig. 5) generating the deformation of the meniscus in Taylor's cone [12].

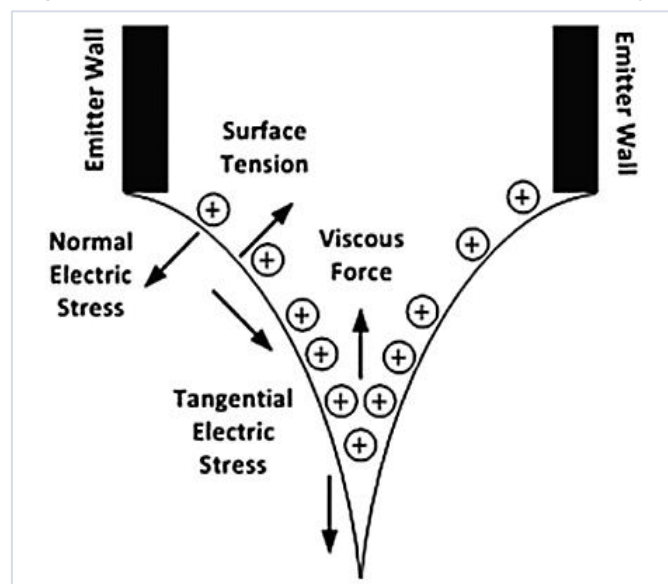


Fig. 5 | Forces within the drop.

Once exceeding the surface tension of the liquid drop, the ejection of apical liquid jets occurs. As a consequence, tiny droplets are deposited on a limited area of the target slide. Once the temperature gradient vanished, the electric field disappears, the liquid drop returns to its initial conformation, as shown in Fig. 6.

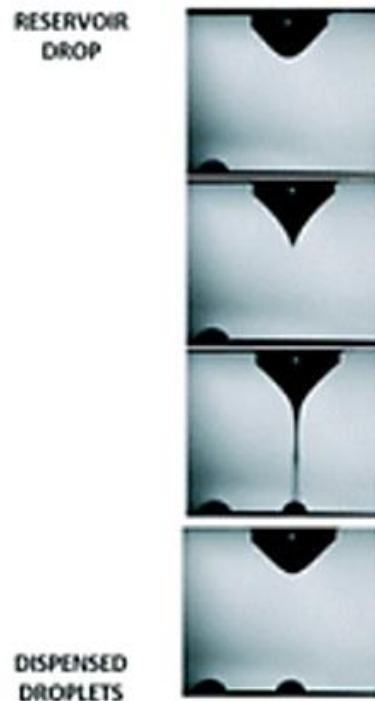


Fig. 6 | Stages of deformation of the mother drop.

The return of the drop to its initial conformation is also due to the charges present in the environment which at a certain point tend to shield the electric field that has formed. The mother drop then delivers liquid periodically until the electric field is active and the separation distance between the base support and the target slide is less than the activation distance [12].

This technique allows one to overcome the drawbacks typically related to the use of nozzles, which are subject to clogging phenomena and to accumulate 70% of the dispensed aqueous droplets dispensed on a restricted area of the target slide [8].

The volume of the liquid mother drop undergoes four main stages of deformation under the application of the electric field, culminating in the

formation of a jet of liquid. Referring to Fig. 7, the first stage corresponds to the neutral condition of the liquid meniscus in which there is a certain surface tension. A pending liquid drop free from electrostatics, aerodynamics and gravitational forces will always assume a spherical shape [16]. This shape corresponds to a minimization of the energy since the molecules on the free surface (liquid-air-interface) have a higher energy than the mass [17]. The increase in the electrostatic potential inside the mother drop determines an increase in the surface charge of the fluid (polarization of the drop) and a loss of surface tension. Charged ions tend to accumulate around the drop and there will be counterbalance between surface tension and electrostatic repulsion. The progressive increase of electrostatic potential allows the columbic repulsion between the ions to overcome the surface tension and this will determine the transition from the drop deformation into a convex tip deformation or into a perfect cone with a defined angle. Finally, once a certain voltage threshold has been reached, the Taylor cone enters jet mode, i.e., there is the emission of jets of liquid. The jet created, being a charge carrier, is directed in the direction of the external electric field.

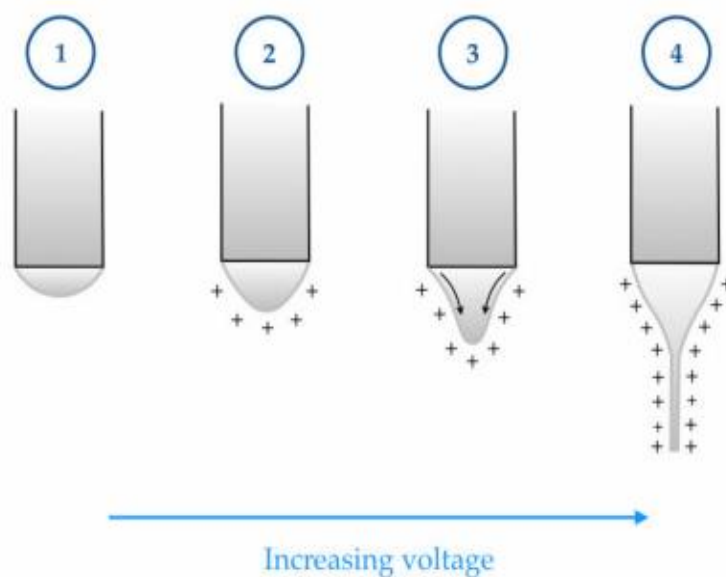


Fig. 7 | Stages of deformation of the drop.

Therefore, the repulsion force must be such as to overcome the surface tension force with which the meniscus of the drop is held to the capillary. If the surface tension is too low, the liquid will form satellite droplets before a stable jet can form, due to a longer setting time. If, on the other hand, the surface tension is too high, the electrostatic force applied is not sufficient to generate the jetting and there is only a pulsation of the meniscus [16]. As in any pointed structure of a conductor, the external field is greater at the tip than the bulk, which is why it will be the area in which there will be ejection [16].

The dependence of the deformation of the drop on the intensity of the electric field is very strong as it has been observed that the drop deforms much more when the voltage is increased. The electric field is therefore the variable that most influences the stretching of the drop.

The Taylor cone is influenced by various factors and the most relevant are:

- flow rate: at high flow rates the electric field is unable to draw a great volume of droplets;
- applied voltage: manipulating the electric field, it's possible to obtain the classical cone and distort it to various degrees;
- viscosity: droplet formation time increases with higher viscosity so it's important to minimize the viscosity [16];
- conductivity.

The electrical conductivity of the liquid sample significantly influences the behaviour of the electro-hydrodynamic effect. The intrinsic mobility of the charge affects parameters such as the Taylor cone formation time, the

relaxation time and the voltage required to cause the flow (all factors also dependent on viscosity) [16].

Regarding the dielectric fluids, the 'Steady Regime' is established during the electro-hydrodynamic phenomenon, in which the cone has a very slow growth (long charging time) and a more acute protrusion [20] as shown in Fig.8.

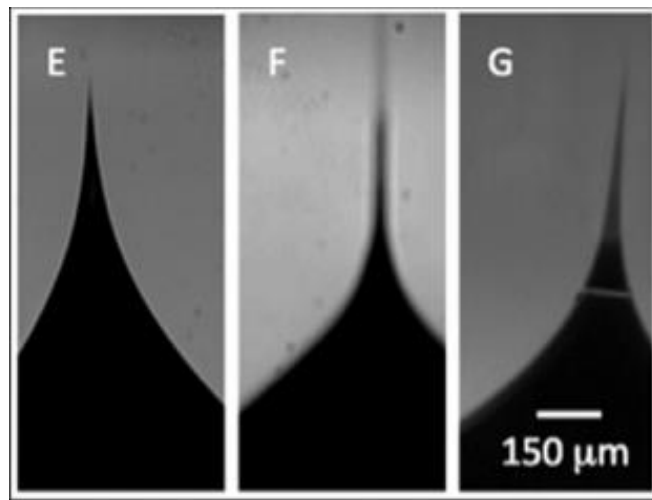


Fig. 8 | Typical meniscus profile in the case of dielectric fluids.

This is because the cone formation is mainly due to convection charges, which move along the surface of the liquid, accumulating at the apex and thus causing the deformation of the meniscus shape. For the re-stabilization of the initial regime is carried out a complete elimination of the temperature gradient.

Regarding the conductive fluids, the 'Pulsating Regime' is established during the electrodynamic phenomenon, in which the cone has a very rapid growth (low charge time) and a limited protrusion (low height) [20], as reported in Fig.9.

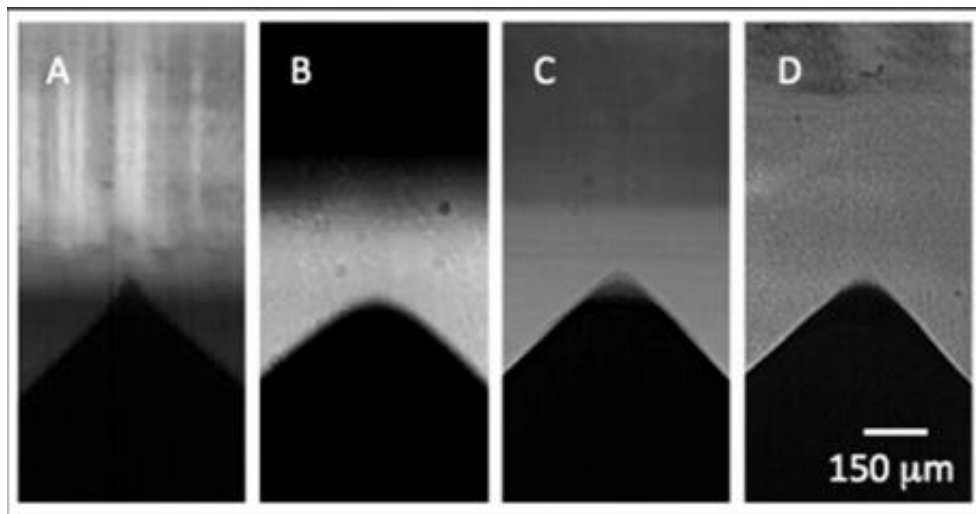


Fig. 9 | Typical profile of the meniscus of a conductive fluid.

This is because the deformation of the drop is mainly due to the conduction charges, which move from the bulk towards the surface, thus being responsible for the spherically symmetrical shape. The re-stabilization of the initial regime is very rapid as the migration of the conducting charges is instantaneous.

1.3 EHD PRINTING CONFIGURATIONS

Electro-hydrodynamic jet printing (EHD) is a direct printing method that allows for nano-dispensing of liquids by having versatility in the inks it can print and reaching a resolution below the nanoscale. It is a non-contact printing technique [16] that works by applying an electric field to induce droplet ejection from a mother drop.

There are various types of configurations based on EHD.

The Classic-EHD configuration is based on the use of an extractor electrode and a source nozzle (between these an electric field is established) and it is the latter that repels the liquid (Fig. 10). Droplets are produced with a size smaller than that of the nozzle [21].

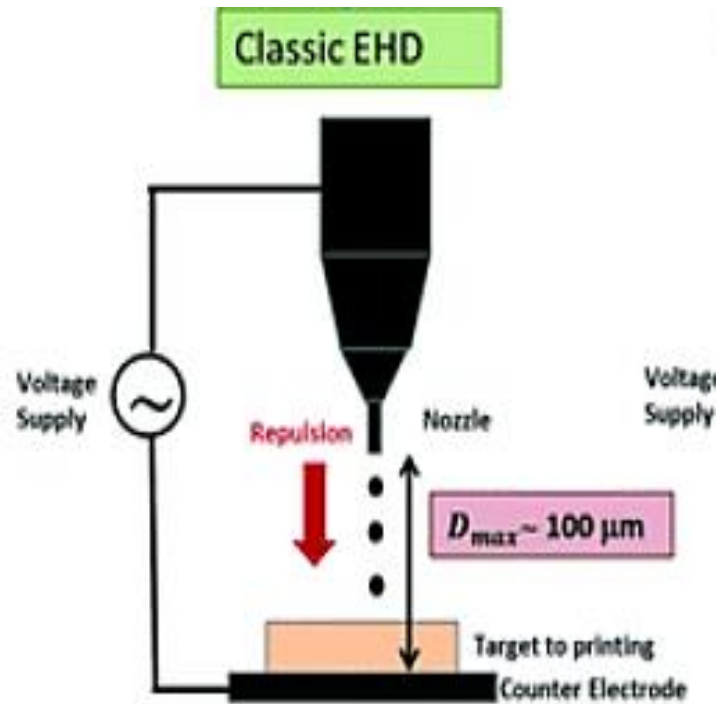


Fig. 10 | Classic-EHD configuration.

In terms of printing, it has numerous limitations such as: use of external electric fields through electrodes, presence of nozzles which is responsible for clogging phenomena, it is not possible to process very viscous liquids (due to issues related to jetting accuracy [21]), use of a thin substrate as it is not necessary to attenuate the intensity of the electric field that hits the meniscus of liquid, and finally does not make the device ready for use.

Another EHD-based configuration is called here Classic Pyro-EHD, with which many limitations of the classic configuration are overcome. There is a ferroelectric crystal in contact with the target substrate and these are placed at a distance from the support that contains the mother gob (Fig. 11).



Fig. 11 | Pyro-EHD configuration.

This configuration is related to the pyro-electrodynamic jet system (p-jet), an innovative technology for an efficient accumulation of tiny solution droplets on the surface of a target slide with the aim at carrying out a highly sensitive detection of the biomolecules present in solution. This technology allows one not only to exceed the common limits of detection (LOD) by pushing the sensitivity below 1 pg/mL but also to significantly reduce the volume of solution necessary for performing the analysis [8].

The use of the pyroelectric effect allows one to avoid the application of the external electric field through electrodes and circuits. Moreover, this configuration is nozzle-free with consequent removal of clogging-related issues. Furthermore, this allows one to process very viscous liquids, where the range of produced droplets goes from microns to hundreds of nanometres [21] and to avoid limits on the type of material, thickness and geometry of the receiving substrate [8].

An innovative aspect of the p-jet technique is the exploitation of the pyroelectric effect in lithium niobate (LN) crystals, where the surface charge generated by an appropriate thermal stimulus makes it possible to print several overlapping droplets on a restricted area of the receiving slide [8]. In fact, the electric field induces a charge on the pending meniscus and, as a consequence, a repulsive Coulomb force which deforms the liquid into a so-called Taylor cone [8] and, when exceeding the surface tension of the fluid, makes it to eject tiny droplets.

However, limitations exist for some kinds of applications. For example, the thickness of the receiving substrate may attenuate significantly the intensity of the electric field before reaching the mother sample drop, thus limiting the types of receiving slides [21].

Another configuration based on EHD is called here Forward Pyro-EHD configuration, where the stimulated ferroelectric crystal is placed behind the mother drop support instead of the receiving substrate (see Fig. 12).

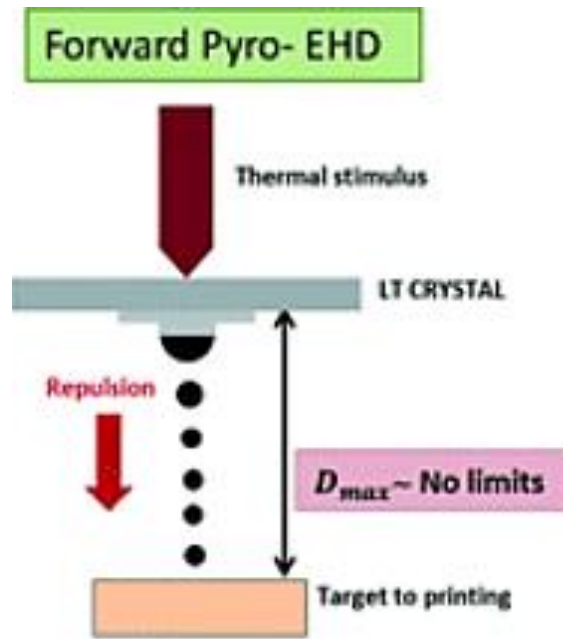


Fig. 12 | Forward Pyro-EHD configuration.

In this configuration there is no limitation on the thickness of the target substrate and on the working distance between the mother drop and the substrate itself. As a direct consequence, this method allows to have devices ready for use [21].

Therefore, the advantages of the pyro-electrodynamic jet system, which make it innovative compared to ordinary methods, are the following:

- nozzle-free which avoids expensive and time-consuming production, dead volumes, damaging clogging [20] of the orifice;
- no dependence of the droplet diameter on the size of the nozzle aperture;
- possibility of accumulating biomolecules in very dilute solutions through tiny droplets, pushing the detection limit under hundreds of aM [22];
- possibility of loading relatively small volumes of sample (down to half microliter) [13];

- the use of the intrinsic electric field generated by the ferroelectric crystal allows one to avoid the application of the high voltage through cumbersome electrodes and circuits in contact with sample target slide [8];
- good reproducibility of the ejected droplets [3].

A further pyro-electrohydrodynamic configuration involves the photovoltaic effect using a lithium niobate crystal doped with Fe ($\text{LiNbO}_3:\text{Fe}$), which once irradiated by a visible light source leads to the ejection of tiny droplets [14]. The photovoltaic effect allows the generation of remarkably high electric fields [15] for moderate or low levels of light excitation. The photovoltaic effect is associated with optical transitions from localized states of impurities, such as $\text{Fe}_2^+/\text{Fe}_3^+$ or $\text{Cu}^+/\text{Cu}_2^+$, and with directional electron migration along the polar axis (photovoltaic current) [14]. While the photovoltaic effect is activated for any light intensity [14], the pyroelectric effect is activated for high light intensities when the crystal heats up due to the absorption of Fe impurities. In this way, direct heating is avoided and visible light is used. The jet direction and thickness can be changed adjusting appropriately the power and the direction of the light emitted.

Chapter 2

MATERIALS AND METHODS

2.1 SETUP DESCRIPTION

The experimental tests were carried out using the **classic Pyro-EHD configuration** with the insertion of a pin. In particular, the lithium niobate ferroelectric crystal in wafer form is placed in contact with the target slide on which point thermal stimuli will be generated [9]; these are located at the bottom. In front there is a polymeric support with an orifice at a certain distance from the target slide; it is important that there is no contact between the polymer support and the target slide. A pin is placed inside the orifice (Fig. 15).

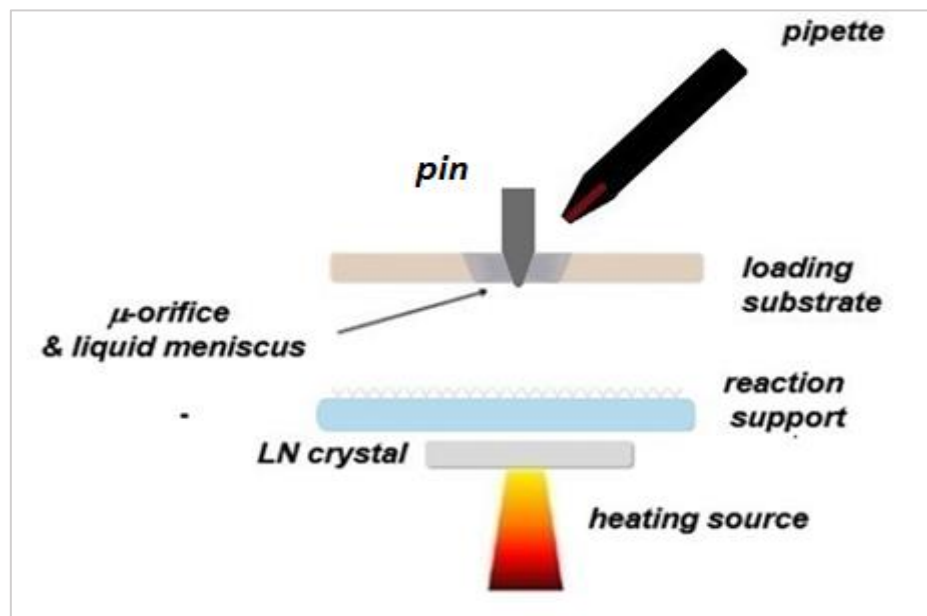


Fig. 15 | Schematic view of the Pyro -EHD configuration with pin insertion.

The pin not only linearly regulates the rate of accumulation of biomolecules in tiny droplets [3] but also allows to have a smaller surface that is charged through the electric field coming from the lithium niobate and therefore a narrower liquid meniscus; in any case avoid contact with the polymeric support.

The pin therefore allows to optimize the accumulation rate of low abundance biomolecules [3], producing a stable meniscus profile, from which the tiny droplets will be ejected with high reproducibility (Fig. 16).

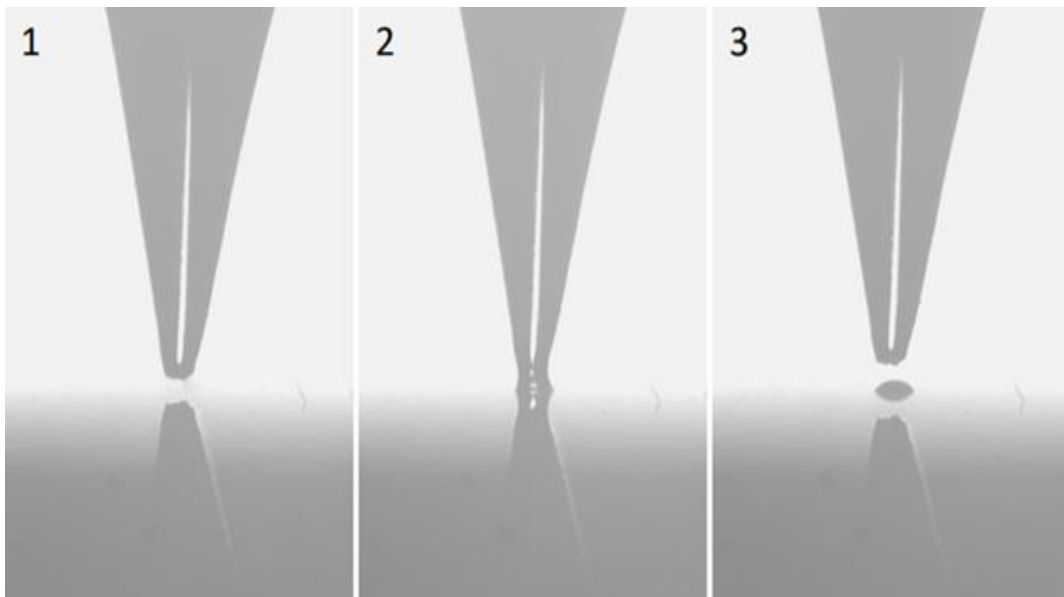


Fig. 16 | Slide view images of the typical droplet formation through the p-jet technique.

The innovation of this configuration lies in the fact that the jetting is obtained through an electrostatic interaction at short distances, thus preserving the spatial precision of the contact printing, but at the same time avoiding the typical connected drawbacks [3].

The volume of fluid, with fluorescently labelled biomolecules inside, is inserted into the orifice with pipettes; the electric field generated by the ferroelectric crystal of lithium niobate (through thermal stimulation) affects the volume of fluid, generating the jetting of droplets on the target slide in front of it. A schematic setup configuration is shown in Fig. 17.

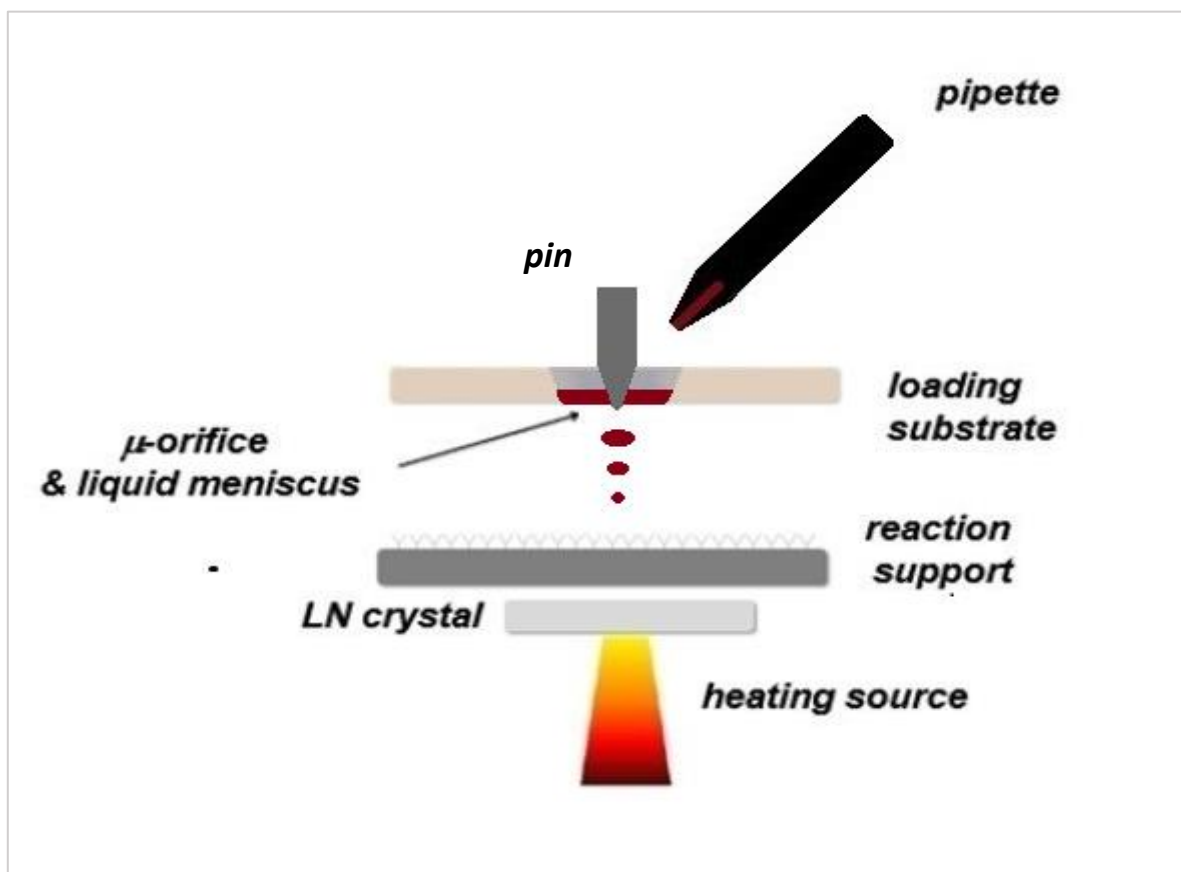


Fig. 17 | Schematic view of the technique used.

The setup used for the experimental tests is the one shown in Fig. 21:



Fig. 21 | Top-down view set-up.

A tungsten wire (transition metal with a very high melting point) placed on a track, is heated by the passage of electric current generated by a power generator (Lab. Grade Switching Mode Power Supply HCS-3300) (Fig. 22).



Fig. 22 | Power generator.

A function generator (Arbitrary Waveform Generator, 20 MHz / function 33220A) allows one to set a unit step function with assigned on and off times (Fig. 23).



Fig. 23 | Function generator.

It is set to the Pulse function as it is necessary to have a predefined period in which the passage of current is ensured / enabled, and another period without current to activate and deactivate the heater with a fixed time interval. The Pulse function (Fig. 24) is a discontinuous function that has zero value (absence of current) for negative arguments and one for positive arguments (presence of current).

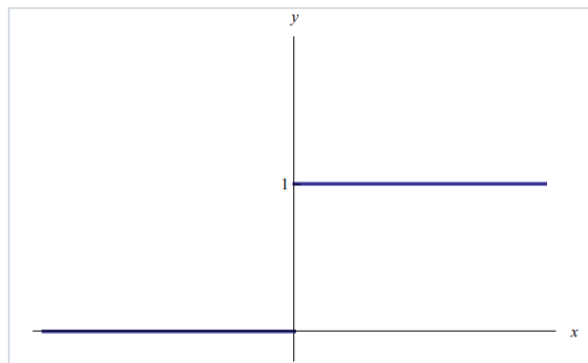


Fig. 24 | Pulse function.

All this to heat the lithium niobate (LN), a rhombohedral crystal belonging to the 3m point group. Due to its unique optical, electronic and physical

properties, LN has a wide range of applications such as non-linear optical devices, compact pyroelectric X-ray sources, piezoelectric resonance biosensors ect. [4]. The only obstacle in the way of its growing industrial use expensive high- quality mechanical processing of LN samples is currently reduced due to implementation of micromachining CNC (Computer Numerically Controlled) [23] and laser micromachining [21] techniques. They were purchased from Crystal Technology Inc. in the form of 3-inch C-cut wafers polished on both sides with a thickness of 500 μm . The wafers were cut into samples of 2 cm^2 by a standard diamond saw.

A led light (Collimated LED for Olympus BX & IX, 1000 mA. M470L4-C1 - 470 nm, 420 mW (Typ.)) acts as a light source necessary for viewing the phenomenology of the drop (Fig. 25).

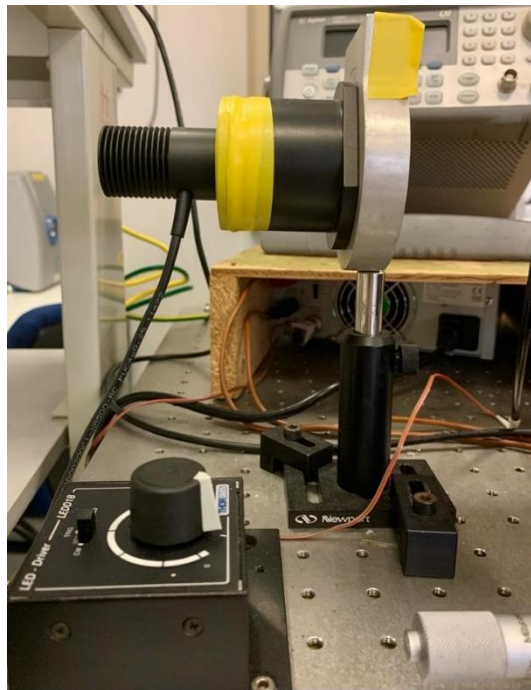


Fig. 25 | Led light.

The target slide is placed on another track which is in contact with the tungsten wire and is the surface on which the droplets with biomolecules are spotted.

In front of a certain distance, the support with orifice is placed inside which the pin is inserted (Fig. 26). Once the support has been mounted with the pin, the alignment of the pin with the process takes place using the positioners; this can be checked by means of the objective placed in front of it.

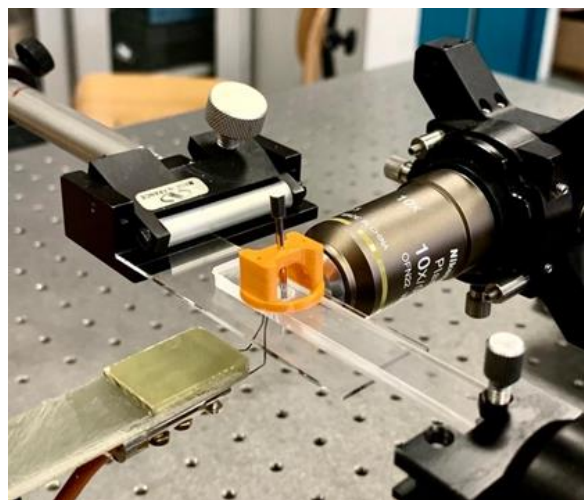


Fig. 26 | Support front view with pin.

The pin used is a Microarray Printing Pin MP3 (Fig. 27).



Fig. 27 | Pin view.

The pin with a diameter of 50 μm has the following measures (Fig. 28):

- internal opening equal to 20 μm ;
- arm thickness equal to 30 μm ;
- total width of the pin tip equal to 80 μm .

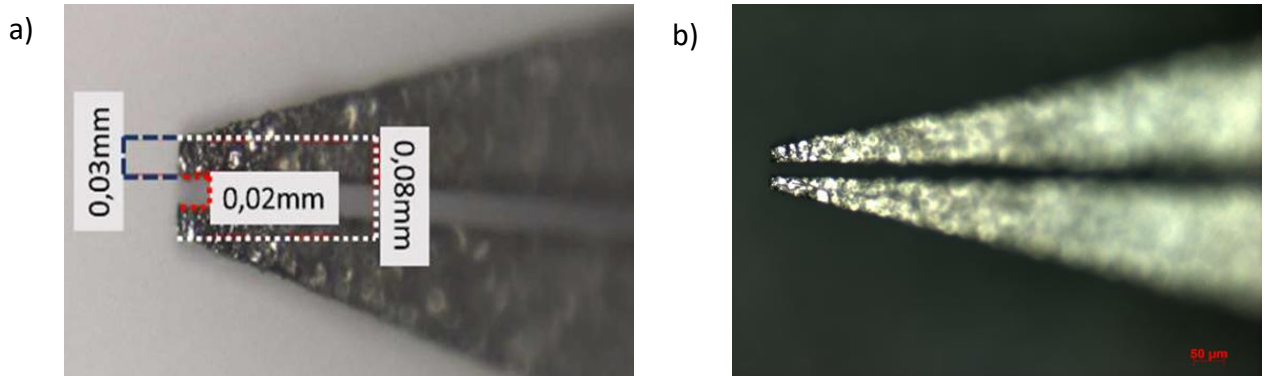


Fig. 28 | a) Pin measurements. b) Pin diameter.

When used under conventional contact printing modality, the pin ensures the following features:

- spot diameter: 100 μm
- absorption volume: 0.1 μl
- volume dispensed: 0.7nl
- minimum spot spacing: 120 μm .

The objective (MY 10X-803 - 10X Mitutoyo Plan Apochromat Objective, 436 - 656 nm, 0.28 NA, 34 mm WD) is placed in proximity of the video camera (Y Series High Speed Digital Camera- IDT Vision) (Fig. 29) which allows one to observe in real time the phenomenology of droplet deposition.

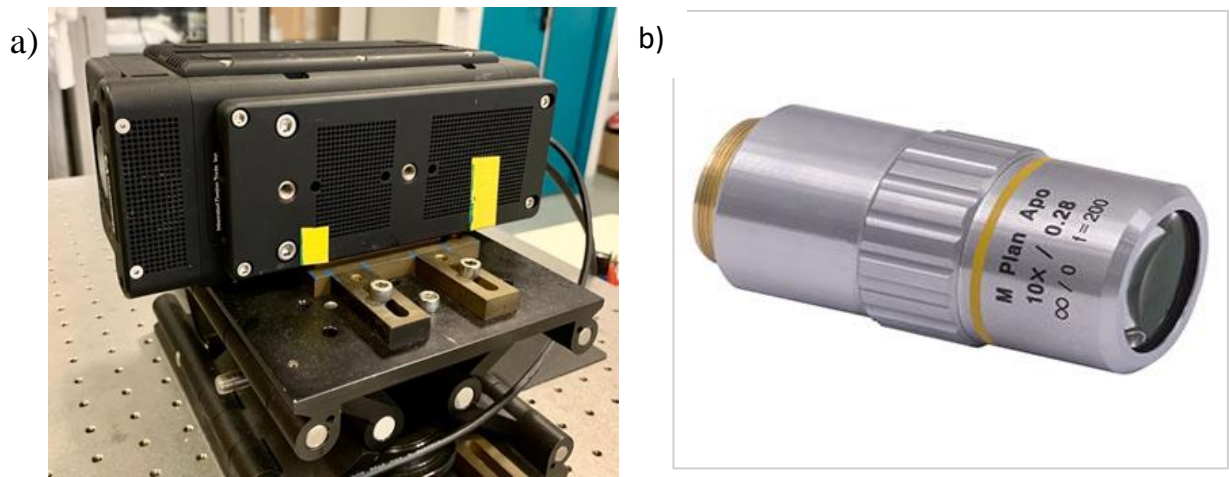


Fig.29 | a) Camera. b) Lens.

2.2 SAMPLE SOLUTION AND SLIDES

The experimental tests were carried out with a solution consisting of a fluorescence-labelled secondary antibody dissolved in synthetic urine. The synthetic urine serves to simulate the conditions of the body fluid. The artificial urine solution used is Biochemazone BZ325 (Fig. 18).



Fig. 18 | Biochemazone BZ325 synthetic urine.

It is a sterile solution with a pH of 4.6, stored at 4 degrees, transported at room temperature and with the following composition:

- Ammonium Chloride
- Calcium chloride dihydrate
- Magnesium Sulphate
- Potassium Chloride
- Sodium Chloride
- Sodium Phosphate, dibasic
- Sodium Citrate
- Sodium sulfate decahydrate
- Sodium phosphate monobasic monohydrate

The fluorescent probe was a secondary antibody conjugated with a fluorophore, Alexa Fluor Plus 647 (cat. N. 111-606-045, Jacksonimmuno) (Fig. 19):



Fig. 19 | Alexa Fluor Plus 647.

This is bought in powder form and it is dissolved in dH₂O with 50% Glycerol (G9012, Sigma-Aldrich), to preserve the stability of the secondary antibody, at 20°C.

The solution is mixed gently to ensure solubilization of the powder antibody. The solution has an initial concentration of 0.66 mg/mL and serial solutions were prepared in the artificial urine to obtain the final concentrations of 500 pg/mL and 0.8 pg/mL.

The slides where the spots are made are commercial 1mm thick microscope slides with 2D-Amine functionalization (PolyAn GmbH, Germany) (Fig. 20). The surface is functionalized by amino groups NH₃⁺, for the non-covalent coupling of negatively charged biochemical species by electrostatic adsorption [3].

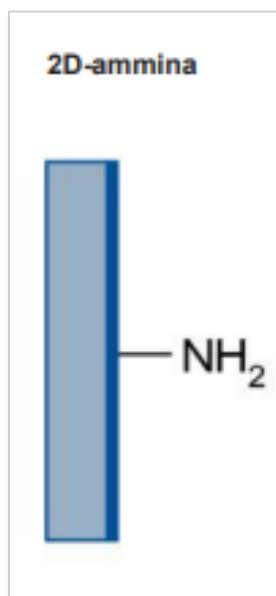


Fig. 20 | 2D-Amine Polyan microarray.

These slides are usually employed in microarray printing and detection of target molecules through immunofluorescence. The molecules binding on

the slide surface is of fundamental importance for the washing steps occurring in the immunofluorescence steps. This thesis work tests the accumulation effect with labelled molecules and therefore the binding capacity of the slide is not crucial.

2.3 PIN-CLEANING

Both pin and support were washed and dried appropriately to ensure that they are free of any solution residue from previous experiments. They are cleaned in washing solution for five minutes in the Transonic T 310 ultrasound bath (Fig. 31). The wash solution was 2% commercial solution in distilled water.



Fig. 31 | Elma Transonic T310 ultrasound bath.

They are then placed inside a Shel Lab oven (Fig.32) for five minutes at 40 °C; to remove any residue from the washing step.



Fig.32 | Oven Shel Lab.

2.4 SPOT ANALYSIS

The spots on the slides were analysed by a commercial microarray fluorescence scanner InnoScan 710 (Innopsys) which picture is shown in Fig. 30.



Fig. 30 | Innoscan 710 scanner.

The imaging system uses the 635 nm laser source to excite the fluorescent molecules and two digital photomultipliers (PMTs) to record the optical signal emitted by the molecules.

Depending on the expected spot size and signal strength, four main scan parameters can be adjusted:

- resolution (from 3 to 40 microns);
- detection speed of the laser on the slide (from 10 to 35 lines / s) which for dilute solutions is set to the minimum value equal to 10 lines / s;
- PMT gain (linear from 0 to 100%) obtained from the projected image which for diluted solutions is set with the maximum value equal to 100;
- laser power (5 and 10 mW) which for diluted solutions will be set to the minimum value equal to 5mW.

Through the Mapix software connected to the scanner (the scanner is controlled via a TCP / IP protocol), it is possible to view the scan in real time and then view the images in real time during acquisition.

After the scanner has warmed up for about 10 minutes and after the laser has reached the optimum temperature, a scan preview is started (at the minimum parameters) to get a quick and complete image of the microarray; select the area that will be subjected to the complete scan, that is the area that contains the spots made.

Once the parameters discussed above have been set, the full scan is performed. Once finished, the image is acquired in jPeg format and the 16-bit TIFF images (captured by the scanner and quantitatively evaluated by the Mapix software).

Finally, we move on to the analysis of the Tiff image: first a grid is built to distinguish the different spots and then start the process of quantifying the image through 'photometric calculations'.

In a spreadsheet you select the parameters of interest:

- spot's **diameter**.
- **Intensity**: measuring the intensity of the region of interest means adding the intensities of all pixels (excluding the masked ones). This is divided into two categories which are the **Total Intensity** or the sum of the intensity values of all the pixels and **Mean Intensity** or the ratio between the sum of the intensity values of all the pixels and the area of interest [25].
- **Signal/noise ratio (SNR35)**: the fluorescence value is related to the background signal. By background signal we mean the noise / disturbance around the spot; the higher this value, the greater the signal of the spot with respect to what surrounds it. The spots that have a value of $SNR35 < 2$, are not considered in the calculations of mean and standard deviation of the diameter, of the Total Intensity and of the Mean Intensity.

Chapter 3

RESULTS AND DISCUSSION

This chapter reports the results obtained through the experimental tests performed for characterizing the behaviour of the spot intensity and diameter varying the load volume, at different solution concentrations.

Two series of tests were carried out by varying the concentration of the secondary antibody dissolved in the artificial urine, the first at the fixed concentration of 500 pg/mL and the second at 0.8 pg/mL. In particular, the second condition was chosen to test the method under a highly challenging molecule concentration.

For each series of tests, three orifice loading volumes were chosen: the first volume chosen is 12.5 μL , a high volume corresponding to the maximum capacity of the orifice. The second loading volume chosen is 0.5 μL , low volume corresponding to the minimum capacity of the pipette used to load the orifice. The third intermediate volume between the two described above is equal to 2.5 μL and was chosen considering a multiplication factor equal to 5.

For brevity the load volumes are called here “high volume”, “low volume 1” and “low volume 2”, respectively.

3.1 SPOT DIAMETER AD INTENSITY AT 500 PG/ML

For the first test, a volume of solution equal to **12.5 μL** (high volume) was loaded into the orifice and 4 spots were made, each with 40 jets. The loading of the orifice with the pipette took place only once at the beginning of the test, proceeding to exhaust the loaded volume. Figure 33 shows the typical scanner image of the resulting spots, where the numbers indicate the order of deposition.

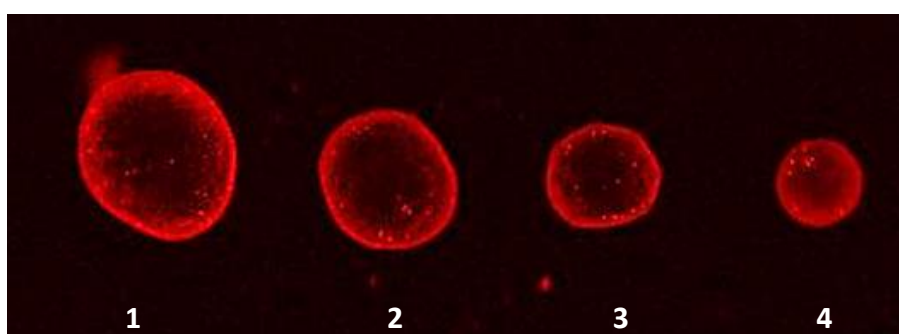


Fig. 33 | Typical scanner image of the spots at 500 pg/mL with volume loaded equal to 12.5 μL .

The scanner images were analysed as usual by Mapix software (see materials and methods) and the resulting values of diameter and fluorescence intensity were processed by Excel for calculating the mean and standard deviation values.

The distribution of the diameter values is shown in the following:

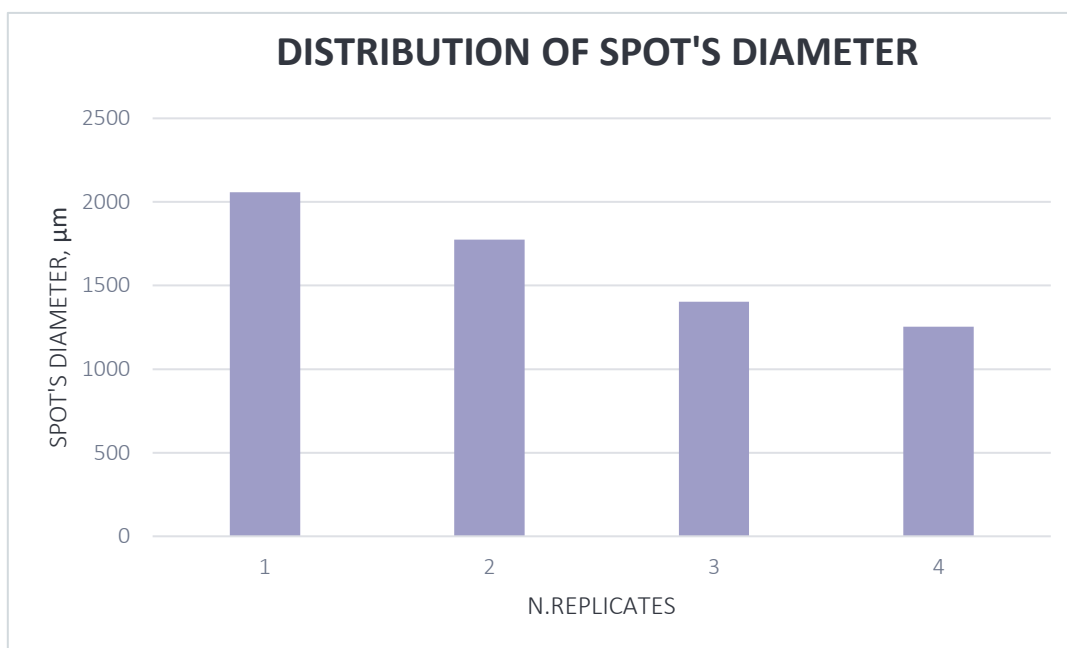


Fig.34 | Distribution of spot diameter at 500 pg/mL with $V_L=12.5 \mu\text{L}$.

Analysing the values of the diameter of the 4 spots, there is a decrease in the diameter going forward with the number of replicates and in particular a decrease of 40% between the value of the first spot and the fourth spot. The coefficient of variability CV was around 36% and was calculated as the ratio between the standard deviation value and the mean value of the diameter, over ten replicates of the experiment. This result shows a poor reproducibility of the spot diameter in case of the “high volume” test.

The distribution of the mean intensity is shown below:

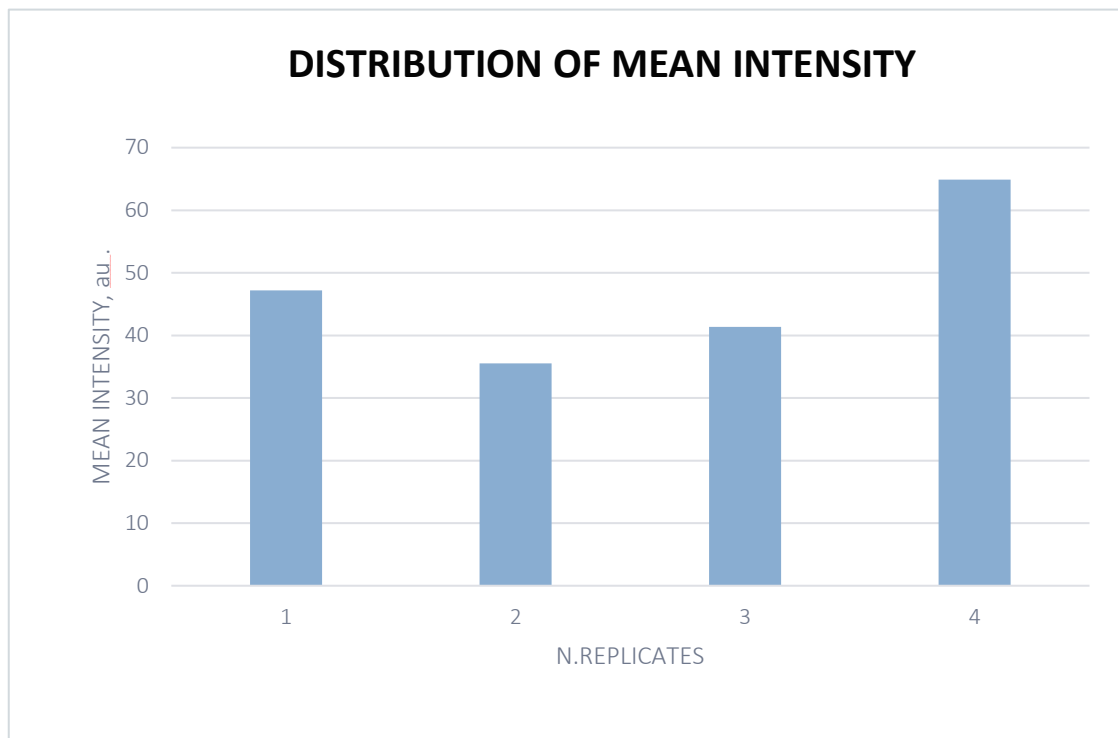


Fig.35 | Distribution of mean intensity at 500 pg/mL with $V_L=12.5 \mu\text{L}$.

A poor repeatability was observed also in case of the spot intensity, with a coefficient of variation of about 51%, over ten replicates of the experiment.

For the second test, a volume of solution equal to **2.5 μL** (low volume 1) was loaded into the orifice and 4 spots were made, each with 40 jets. The loading of the orifice with the pipette took place only once at the beginning of the test, proceeding to exhaust the loaded volume. This was possible as the loaded volume considered is relatively high and hence able to generate up to four spots with 40 jets each. Figure 36 shows a typical scanner image of the of the spots.

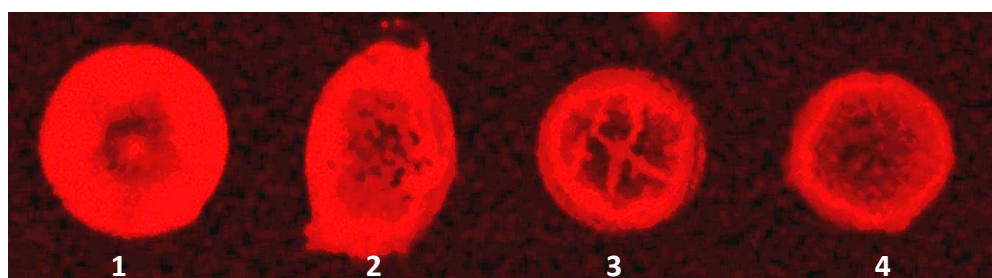


Fig. 36 | Typical scanner image of the spots at 500 pg/mL with volume loaded equal to 2.5 μL .

The distribution of the diameter values is shown in the following:

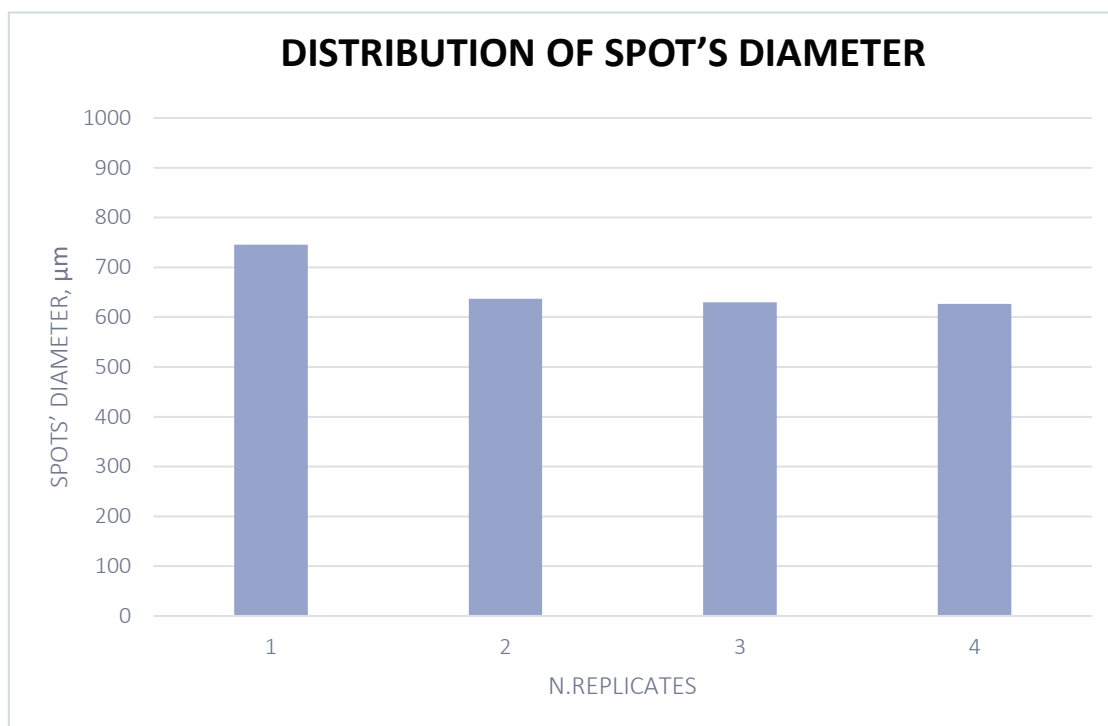


Fig.37 | Distribution of spot diameter at 500 pg/mL with $V_L=2.5 \mu\text{L}$.

The repeatability of the spot diameter appears clearly improved in case of $2.5 \mu\text{L}$ load volume, with a coefficient of variation of about 9% over ten replicates of the experiment. Moreover, a slight decrease of 14% is typically observed from the first spot to the last one.

The distribution of the mean intensity is shown in the following:

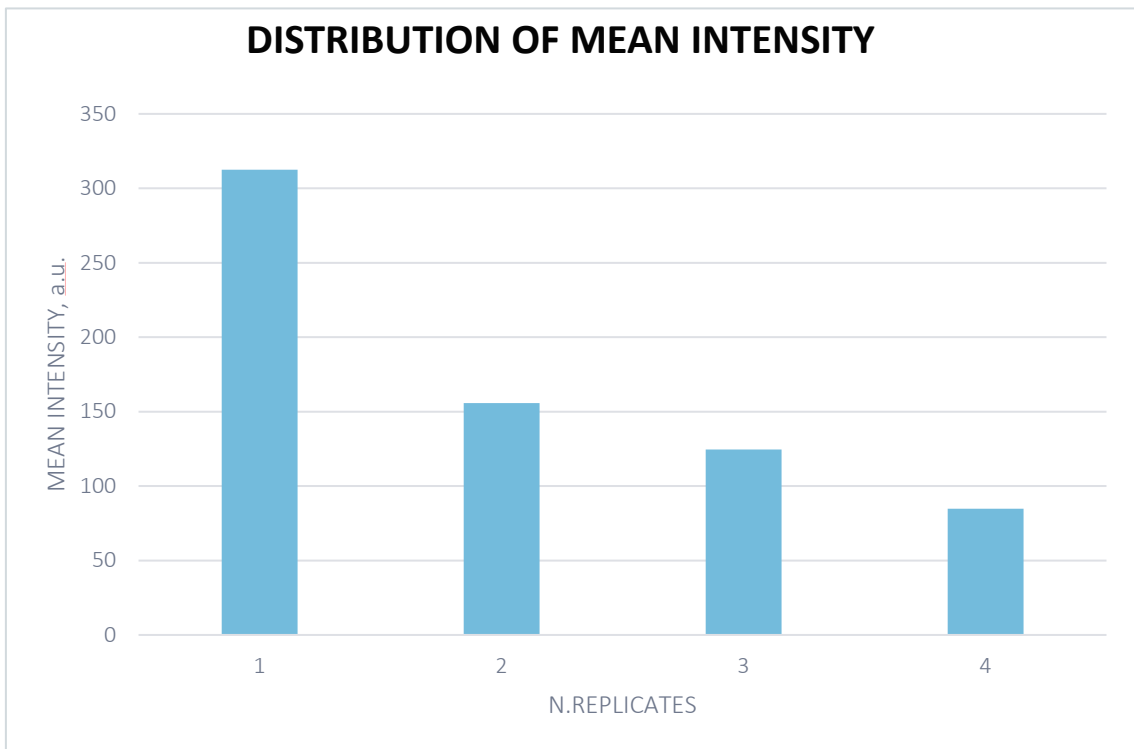


Fig.38 | Distribution of mean intensity at 500 pg/mL with $V_L=2.5 \mu\text{L}$.

The results show a significant decrease of the intensity from the first to the fourth spot, with a variation around 80%. The coefficient of variation was around 59%, over ten replicates of the experiment, thus demonstrating the poor repeatability of the fluorescence intensity.

Finally, for the third experiment, a volume of solution equal to **0.5 μL** (low volume 2) was loaded into the orifice and 4 spots were made, each with 40 jets. The orifice loading with pipette occurred once at the start of the test and once at the fourth spot since the loaded volume is very small and therefore ran out at the end of the third spot. Figure 39 shows the typical scanner image, where the first spot coincides with the first replicate.

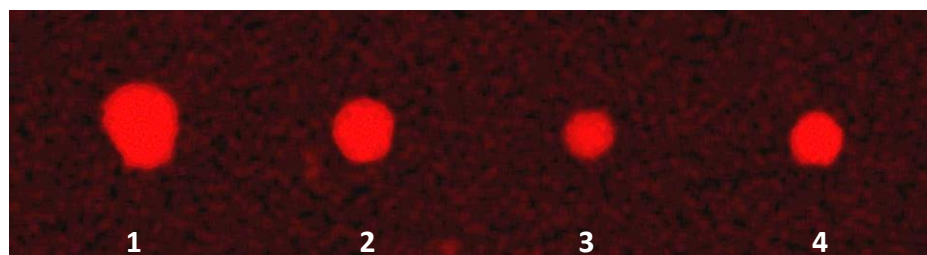


Fig. 39 | Typical scanner image of the spots at 500 pg/mL with volume loaded equal to 0.5 μL .

The distribution of the values is shown in the following:

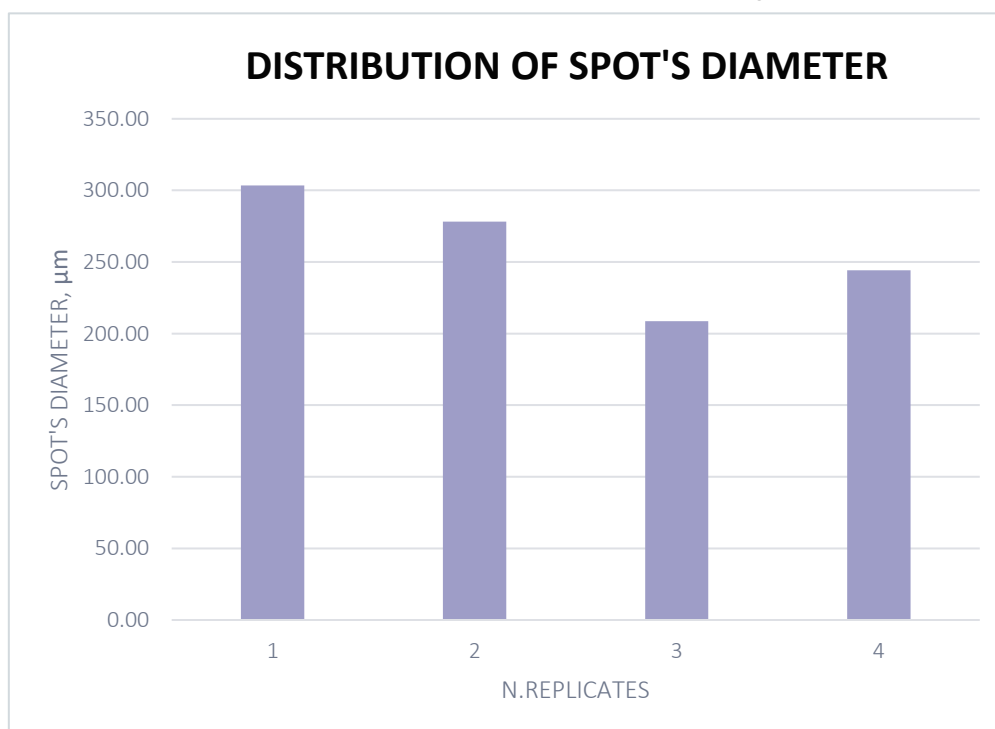


Fig.40 | Distribution of spot diameter at 500 pg/mL with $V_L=0.5 \mu\text{L}$.

A slight decrease of the diameter is observed while emptying the orifice, with a decrease of about 20% between the value in the first spot and that in the fourth spot. The coefficient of variance was around 16%, demonstrating an improved diameter repeatability compared to the previous case at 12.5 μL .

The distribution of the mean intensity is shown in the following:

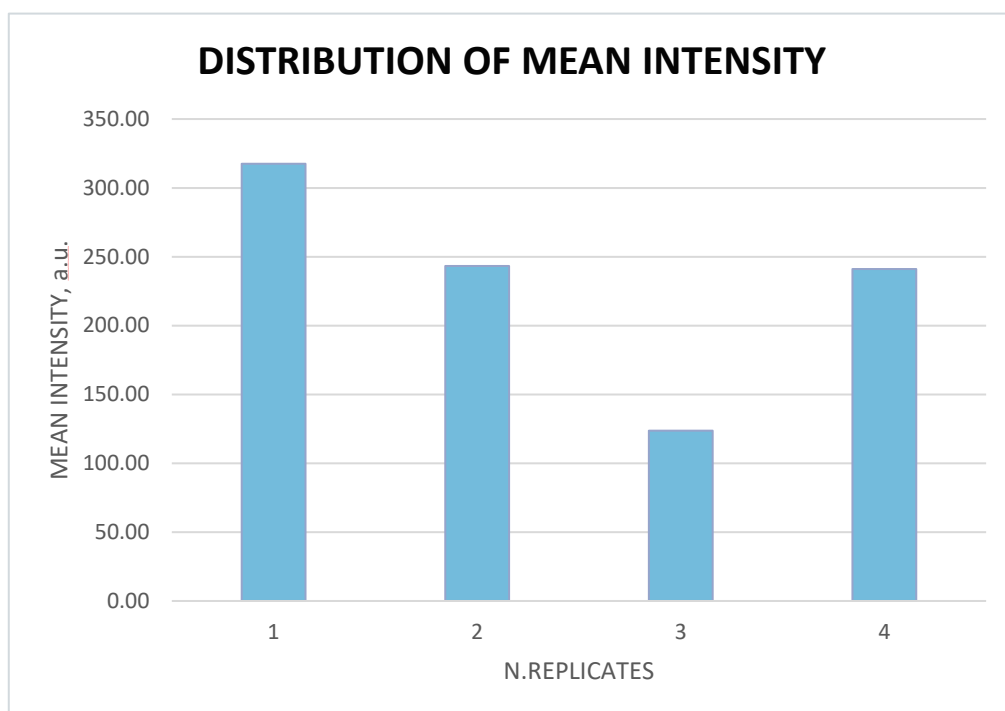


Fig.41 | Distribution of mean intensity at 500 pg/mL with $V_L=0.5 \mu\text{L}$.

The mean intensity of the spot appears to decrease with a variation around 60%. Moreover, the fourth spot shows a significant increase of the signal probably due to the additional loading of the orifice.

The coefficient of variation was around 35% over ten replicates of the experiment, thus showing a non-satisfactory repeatability of the spot intensity.

The figures below show the summary of the results obtained in all of the experiments:

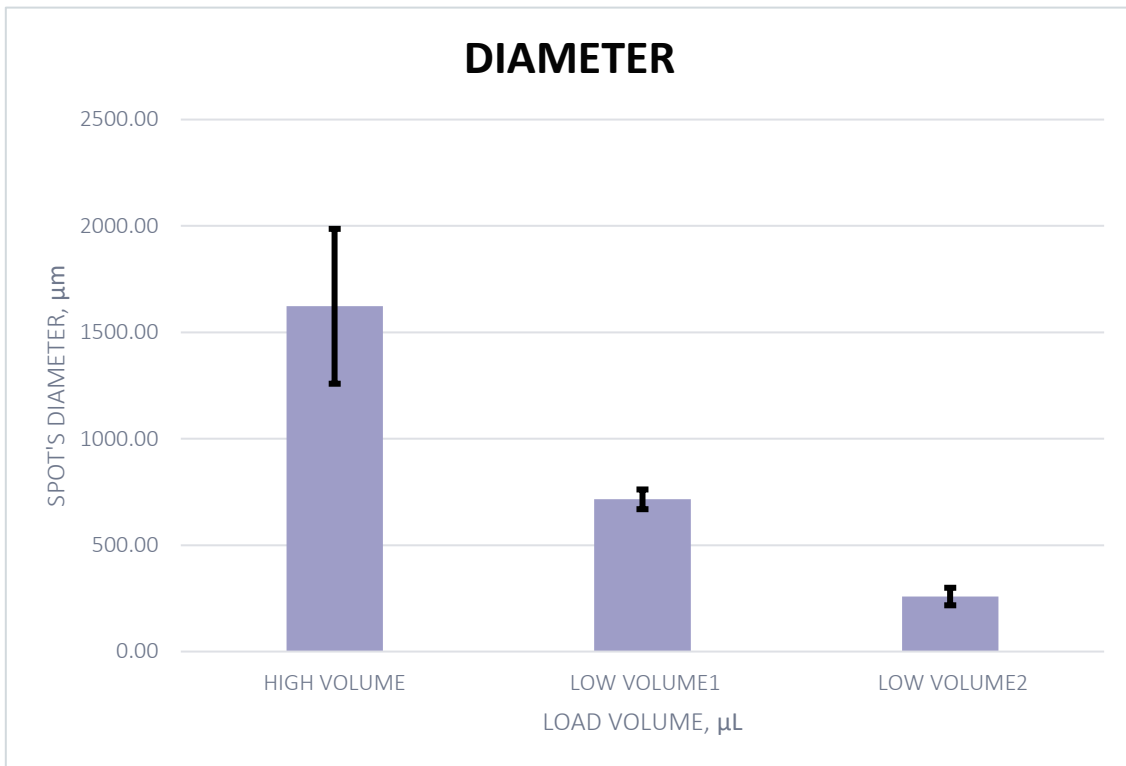


Fig.42 | Distribution of mean diameters at 500 pg/mL.

The overall experiments show clearly that the spot diameter decreases significantly with decreasing load volume. A decrease of about 75% is observed from the high volume to the low volume range. This is probably related to a higher volume of liquid ejected in case of higher load volume, related to the more significant role of the gravity force. Anyway, this is an effect which needs further study in the next future. The spot diameter shows a higher repeatability in case of low volume range.

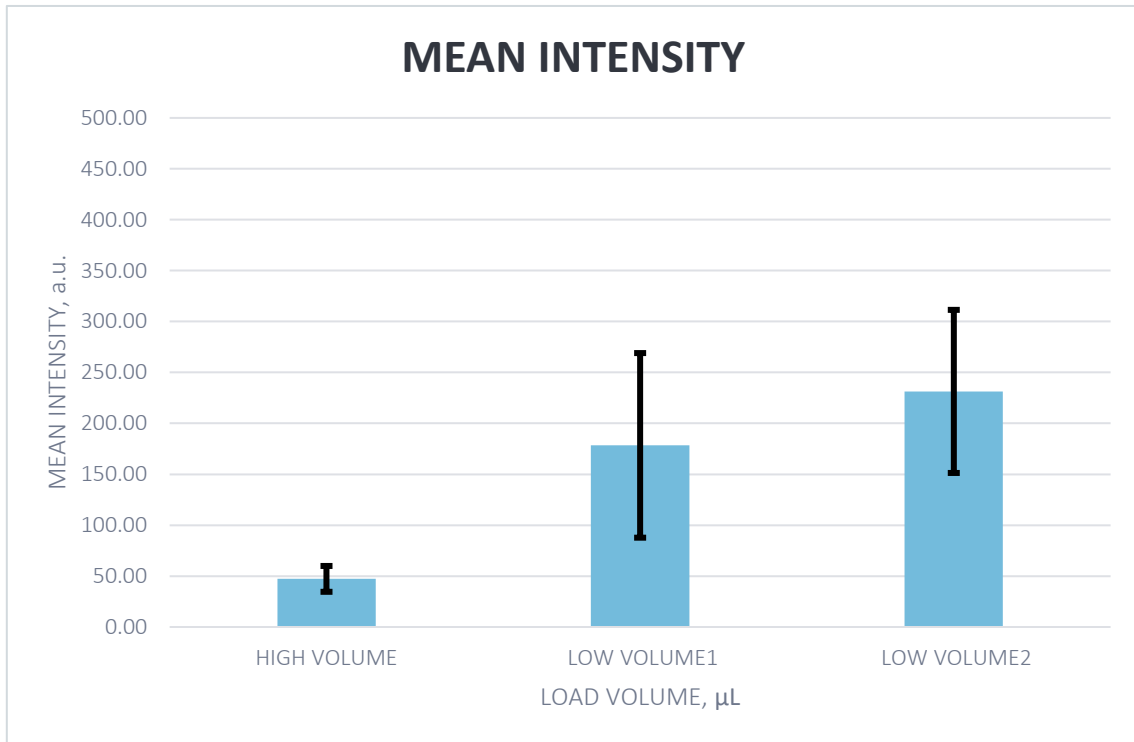


Fig.43 | Distribution of mean intensity at 500 pg/mL.

Regarding the trend of mean intensity, this increases significantly from the high-volume range to the 'low volume' range. There is an increase of about six times between the value of the high volume and that of the low volume 2. This can be explained by the fact that for shorter diameters a mean higher intensity arises due to the ratio over a more restricted area. In summary, as the diameter decreases the mean intensity increases as a result of the higher number of molecules per unit area, thus demonstrating the concentration capability of the technique.

3.2 SPOT DIAMETER AND INTENSITY AT 0.8 PG/ML

For the first test, a volume of solution equal to **12.5 μL** (high volume) was loaded into the orifice and 3 spots were made, each with 40 jets. The loading of the orifice with the pipette took place only once at the beginning of the test, proceeding to exhaust the loaded volume. Figure 44 shows the typical scanner image of the resulting spots, where the numbers indicate the order of deposition.

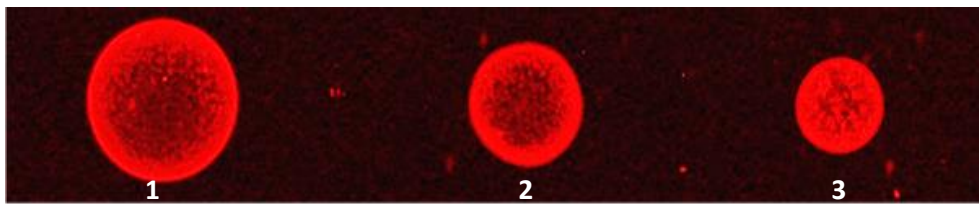


Fig. 44 | Typical scanner image of the spots at 0.8 pg/mL with volume loaded equal to 12.5 μL .

The diameter tends to decrease as the experiment proceeds and the distribution of the diameters is shown in the following:

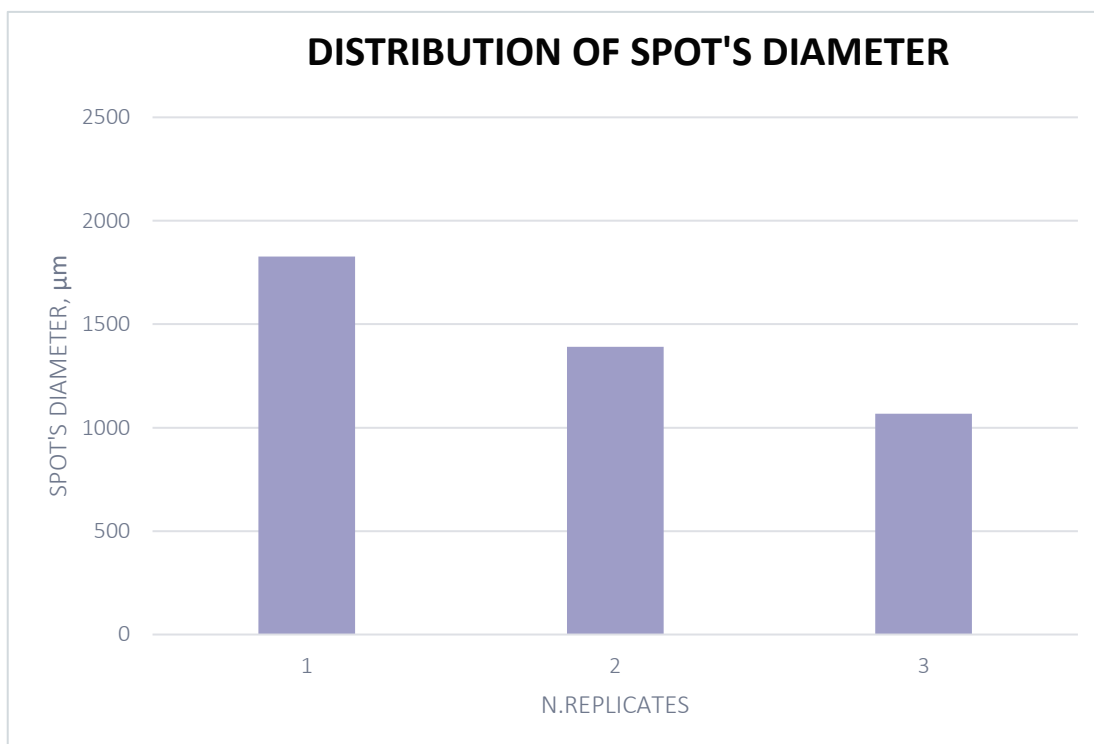


Fig.45 | Distribution of spot diameter at 0.8 pg/mL with $V_L=12.5 \mu\text{L}$.

Analysing the values of the diameter of the 3 spots, there is a decrease in the diameter going forward with the number of replicates and in particular a decrease of 40% between the value of the first spot and that of the third spot. The coefficient of variability was around 37% and this result shows a poor reproducibility of the spot diameter.

The distribution of the mean intensity is shown in the following:

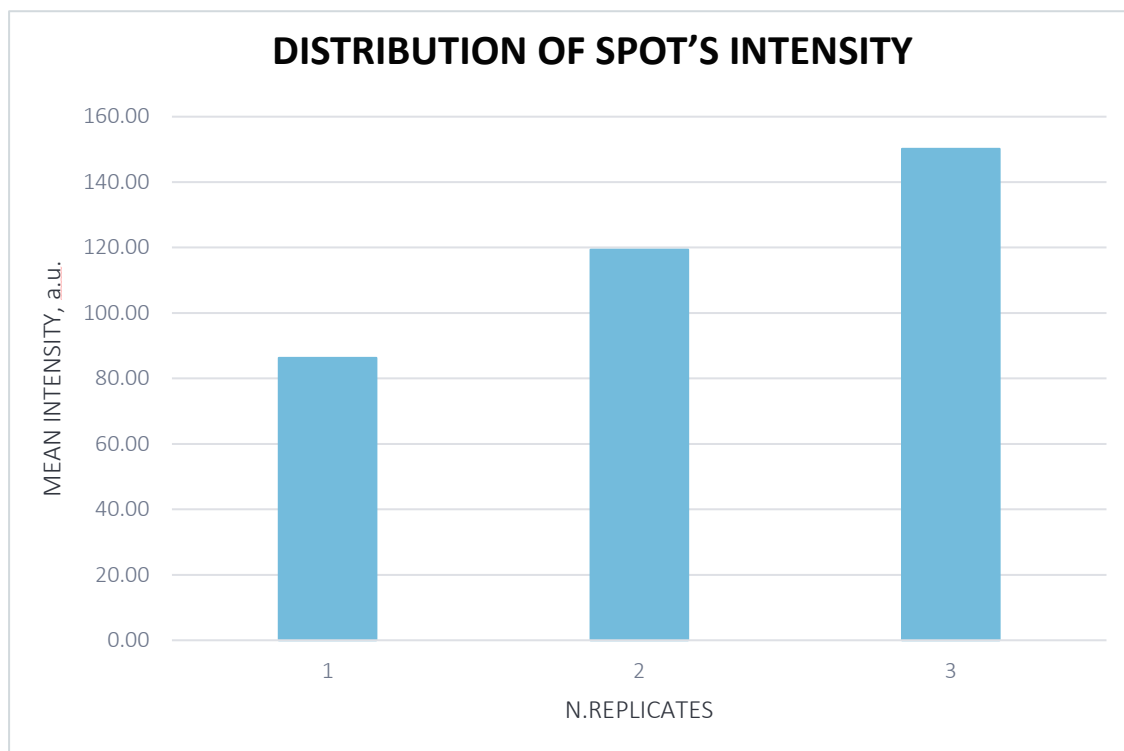


Fig.46 | Distribution of mean intensity at 0.8 pg/mL with $V_L=12.5 \mu\text{L}$.

A poor repeatability was observed also in case of the spot intensity, with a coefficient of variation of about 38%, over ten replicates of the experiment.

There is an increase in the average intensity with the number of replicates; this is explained by the decrease in the spot diameter or as the diameter decreases there is a greater presence of secondary antibody as an increasingly narrow area is considered. Thus, this suggests that for low secondary antibody concentrations in the loaded solution, the narrower the spot area the greater the secondary antibody concentration.

The trends of diameter and mean intensity are the same observed at a concentration of 500 pg /mL.

For the second test, a volume of solution equal to **2.5 μL** (low volume 1) of solution was loaded into the orifice and 4 spots were made, each with 40 jets. The loading of the orifice with the pipette took place only once at the beginning of the test, proceeding to exhaust the loaded volume. This was possible as the loaded volume considered is relatively high and hence able to generate up to four spots with 40 jets each. Figure 47 shows a typical scanner image of the of the spots.

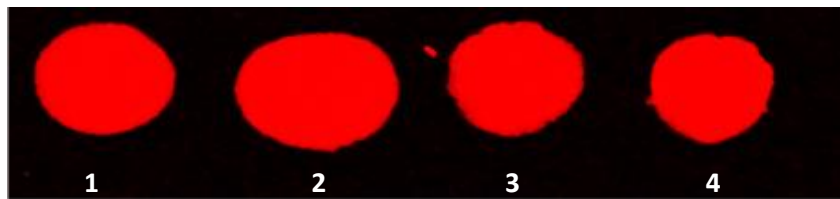


Fig. 47 | Typical scanner image of the spots at 0.8 pg/mL with volume loaded equal to 2.5 μL .

The distribution of the diameter values is shown in the following:

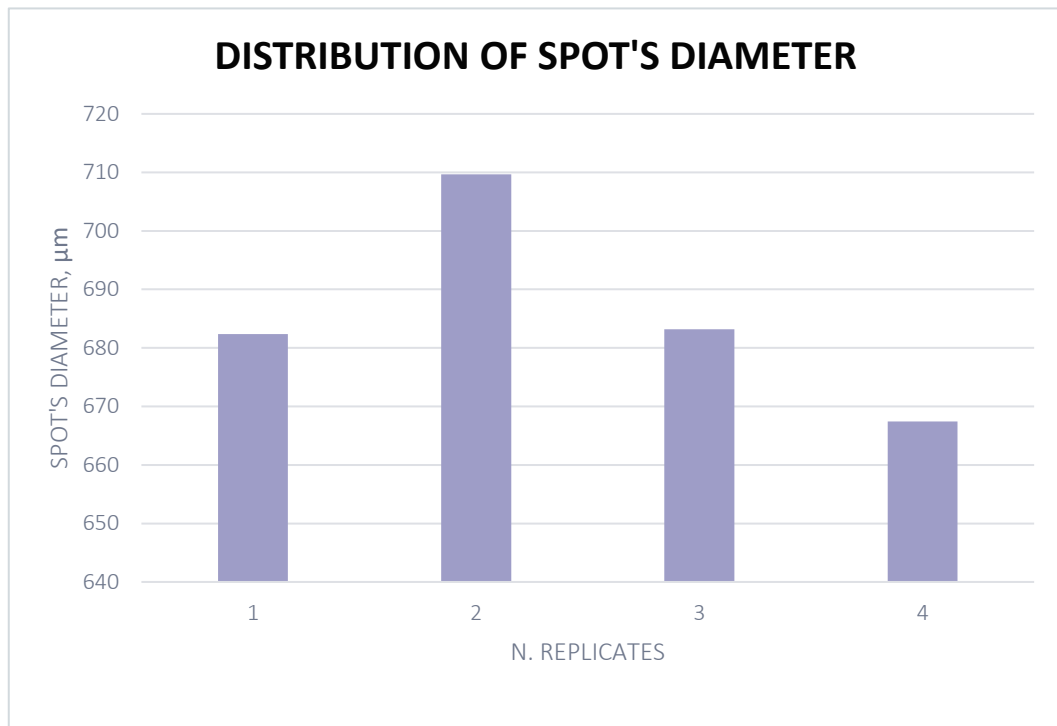


Fig.48 | Distribution of spot diameter at 0.8 pg/mL with $V_L=2.5 \mu\text{L}$.

The repeatability of the spot diameter appears clearly improved in case of 2.5 μL load volume, with a coefficient of variation of about 3% over ten replicates of the experiment.

Repeatability was also observed in the case of 500 pg/mL .

The distribution of the mean intensity is shown in the following:

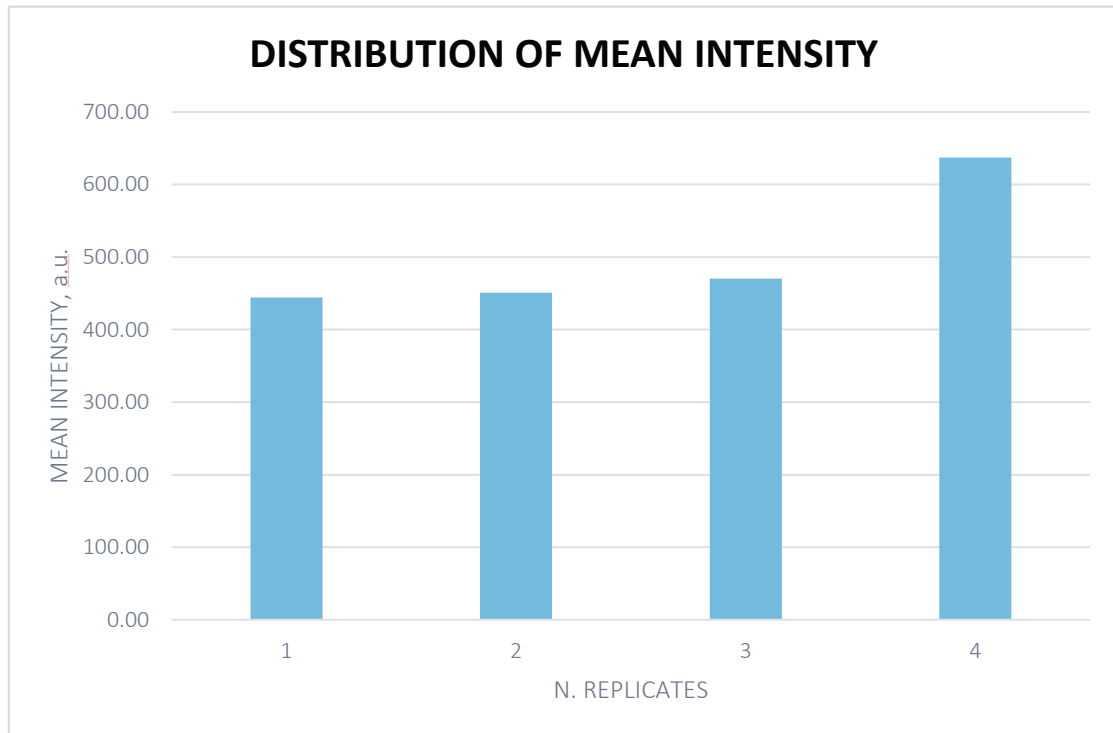


Fig.49 | Distribution of mean intensity at 0.8 pg/mL with $V_L=2.5 \mu\text{L}$.

The mean intensity values for the 4 replicates turn out to be very similar, in fact there is a coefficient of variation of about 3% over ten replicates of the experiment, a value that suggests good repeatability.

In the case in question, an increase in the average intensity is always observed, but less marked than in the case of the loaded volume equal to 12.5 μL . This is explained by considering the trend of the values of the diameter in each spot: in this case we note the strong similarity of all the values of the diameter which therefore differ very little.

Finally, for the third experiment, a volume of solution equal to **0.5 μL** (low volume 2) of solution was loaded into the orifice and 4 spots with 40 jets were made. The pipette orifice was loaded once at the start of the test. Figure 50 shows the typical scanner image of the resulting spots, where the numbers indicate the order of deposition.



Fig. 50 | Typical scanner image of the spots at 0.8 pg/mL with volume loaded equal to 0.5 μL .

The distribution of the diameter values is shown in the following:

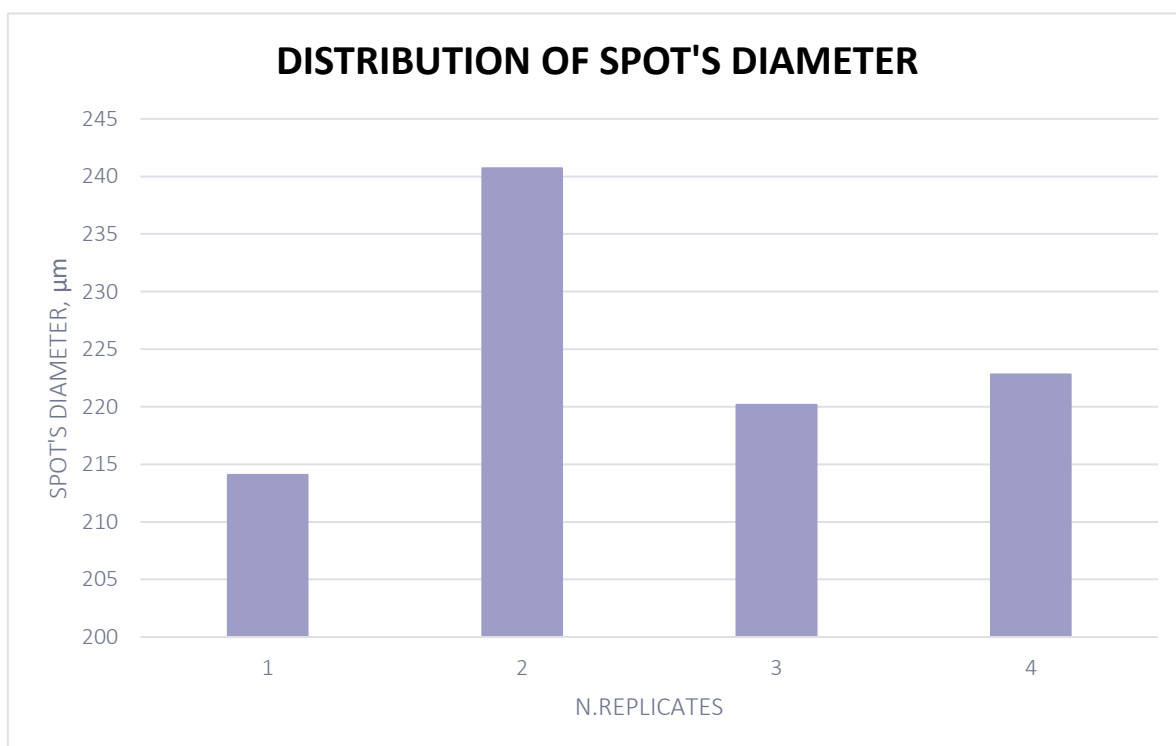


Fig.51 | Distribution of spot diameter at 0.8 pg/mL with $V_L=0.5 \mu\text{L}$.

The values of the diameter for the 4 replicates turn out to be very similar in fact, evaluating the coefficient of variance, this is around 5% demonstrating an improved diameter repeatability.

The distribution of the mean intensity values is shown in the following:

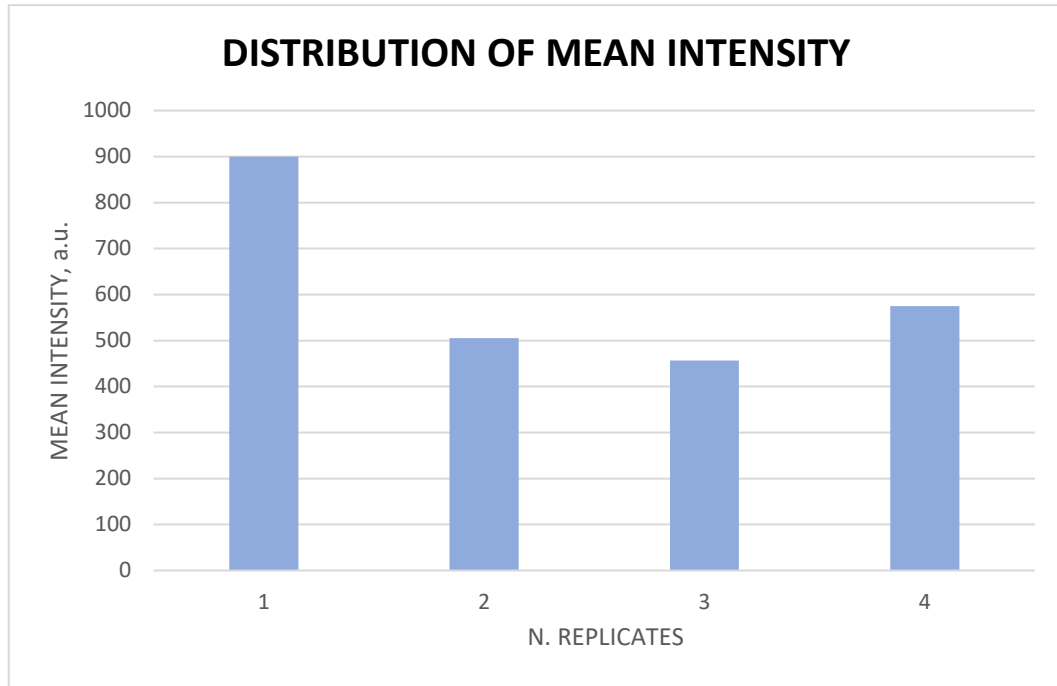


Fig.52 | Distribution of mean intensity at 0.8 pg/mL with $V_L=0.5 \mu\text{L}$.

The mean intensity values for the 4 replicates follow an unclear trend and evaluating the coefficient of variation, this is equal to 37%, a value that suggests bad repeatability.

The figures below show the summary of the results obtained in all of the experiments:

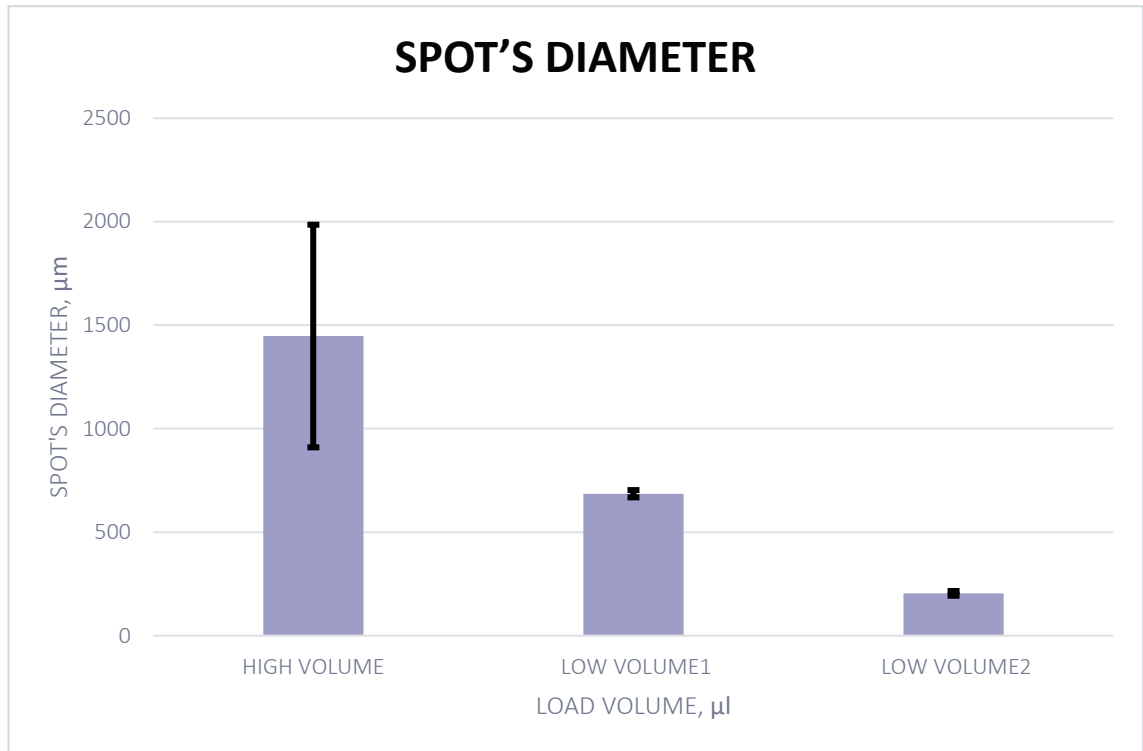


Fig.53 | Distribution of spot diameter at 0.8 pg/mL.

The trends are the same observed in the case of the concentration equal to 500 pg/mL.

The overall experiments show clearly that the spot diameter decreases significantly with decreasing load volume. A decrease of about 75% is observed from the high volume to the low volume range. This is probably related to a higher volume of liquid ejected in case of higher load volume, related to the more significant role of the gravity force. Anyway, this is an effect which needs further study in the next future. The spot diameter shows a higher repeatability in case of low volume range.

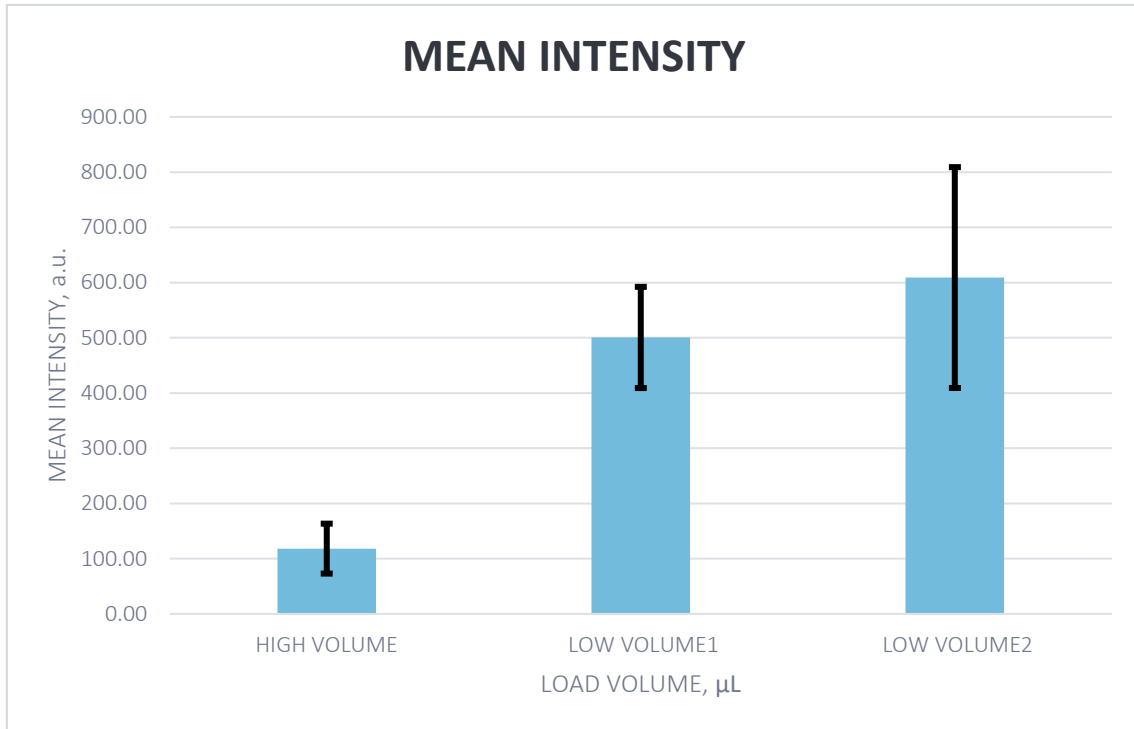


Fig.54 | Distribution of mean intensity at 0.8 pg/mL.

Regarding the trend of mean intensity, this increases significantly from the high-volume range to the 'low volume' range. There is an increase of about six times between the value of the high volume and that of the low volume 2. This can be explained by the fact that for shorter diameters a mean higher intensity arises due to the ratio over a more restricted area.

In summary, as the diameter decreases the mean intensity increases as a result of the higher number of molecules per unit area, thus demonstrating the concentration capability of the technique.

3.3 EFFECT OF THE NUMBER OF JETS

In the framework of the tests at 0.8 pg/ml with a load volume of **0.5 μ L**, further spots with one single jet were produced for a comparative study. The slide with the spots obtained with a single jet is the one shown in Fig. 50-55; the loading is always the one at the beginning of the test.

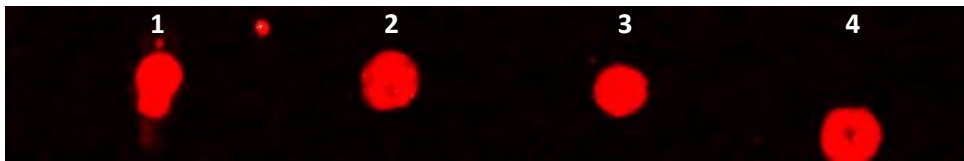


Fig. 50 | Typical scanner image of the spots at 0.8 pg/mL with volume loaded equal to 0.5 μ L.

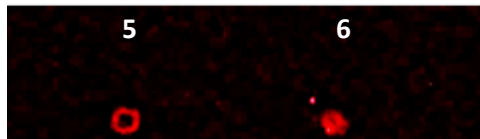


Fig. 55 | Typical scanner image of the spots (1jet) at 0.8 pg/mL with volume loaded equal to 0.5 μ L.

Considering separately the mean and standard deviation values for 1 jet and 40 jets respectively, the following distributions were obtained:

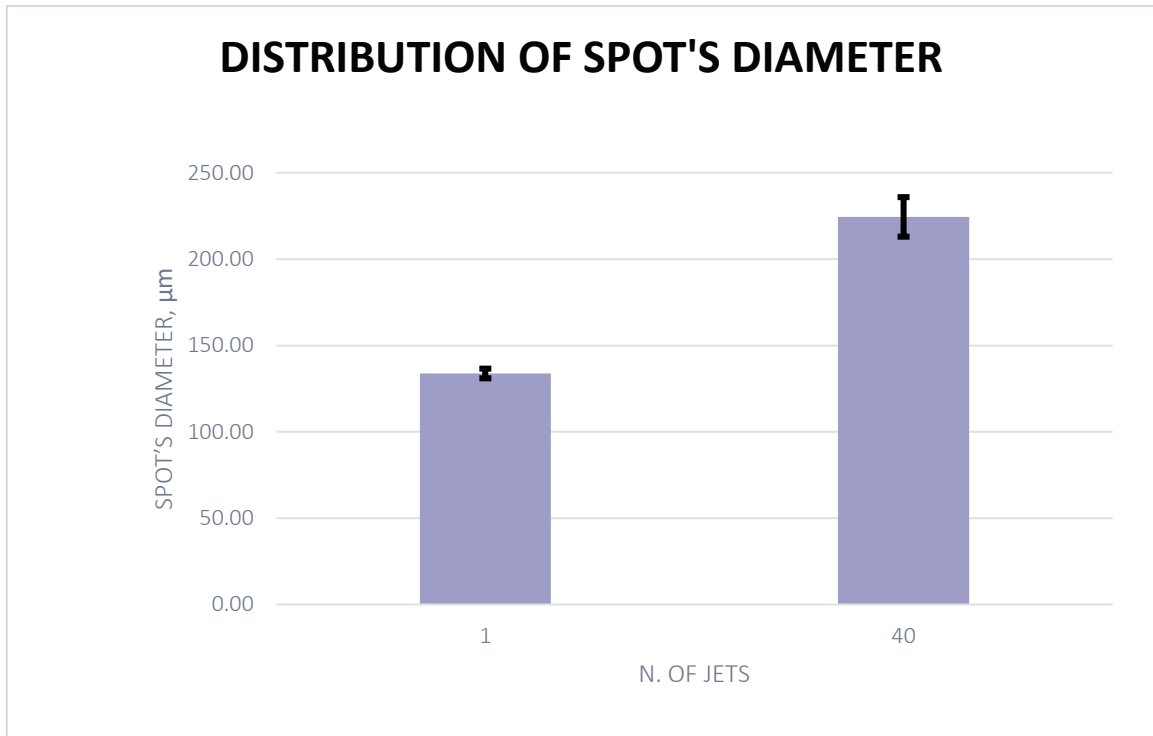


Fig.56 | Distribution of spot diameter at 0.8 pg/mL with $V_L=0.5 \mu\text{L}$.

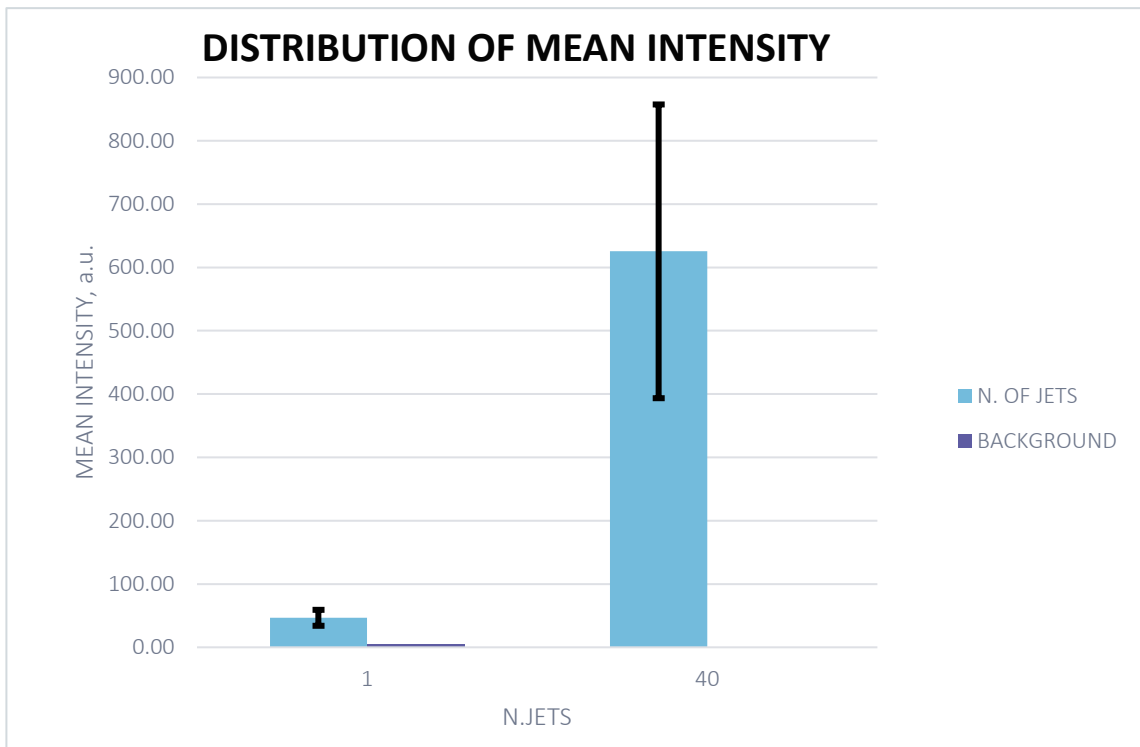


Fig.57 | Distribution of mean intensity at 0.8 pg/mL with $V_L=0.5 \mu\text{L}$.

By analysing the two trends, it can be seen that the diameter undergoes an increase of 1.7 times, passing from 1 jet to 40 jets, exhibiting good repeatability; the mean intensity undergoes an increase of 15 times passing from a jet to 40 jets this can be justified by the accumulation effect.

3.4 VOLUME LOADED AND VOLUME DISPENSED

During the first test (Fig.33), when the concentration is set at **500 pg/mL** and the volume of solution loaded into the orifice is equal to **12.5 μL** , another aspect is investigated. There is an evaluation of the volume dispensed in relation at the volume loaded; this evaluation is made for each replicate.

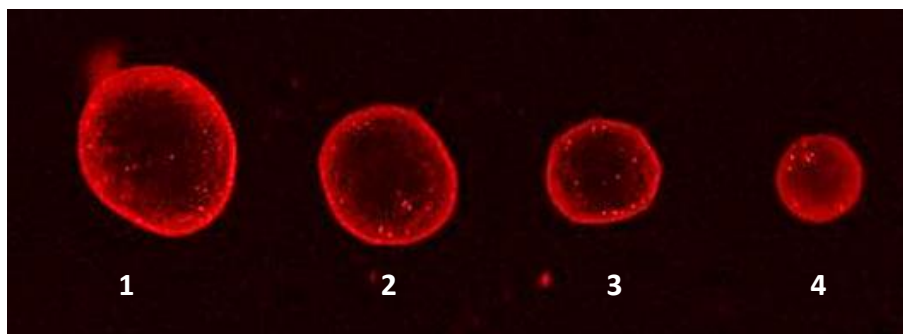


Fig. 33 | Typical scanner image of the spots at 500 pg/mL with volume loaded equal to 12.5 μL .

By evaluating the volume dispensed in the different replicates, the distribution is shown in the following:

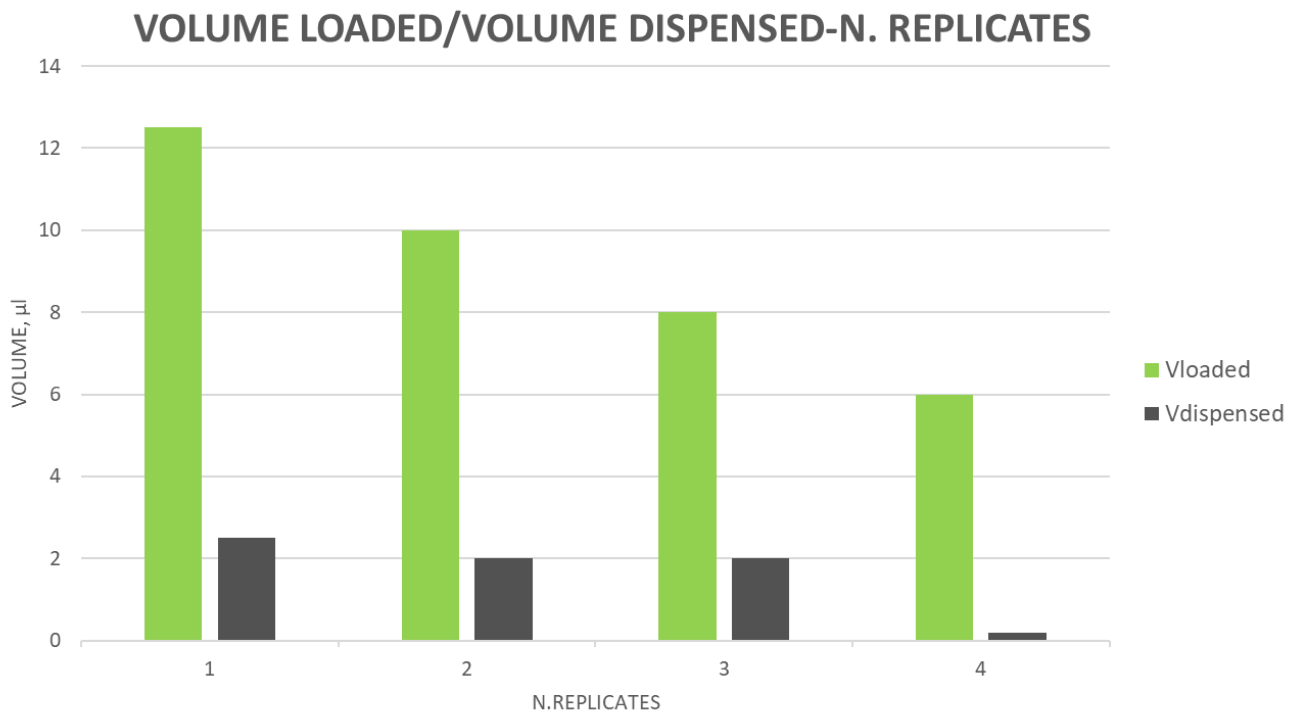


Fig.56 | Distribution of volume loaded and volume dispensed.

It's possible to observe that there is a big leap from the third to the fourth spot.

Chapter 4

CONCLUSIONS AND FUTURE PERSPECTIVE

Through the experimental tests carried out it has been observed that passing from the high-volume range to the low volume range, the diameter decreases by about 75% as with the decrease in volume smaller droplets are generated while the mean intensity increases by a factor of 6 as due to the phenomenon related to accumulation (accumulation effect), having smaller diameters there is a smaller area on which the mean is evaluated intensity.

Evaluating the repeatability, only the diameter is repeatable in the case of low volume range exhibiting a CV <10%; in the case of the high volume range the CV is too high and therefore the repeatability is not acceptable.

For the mean intensity for no volume a good repeatability was observed.

The same behaviours were observed for both 500 pg/mL and 0.8 pg/mL.

As regards the effect of the number of jets, passing from 1 jet to 40 jets in the case of a loaded volume equal to 0.5 μ L with a concentration set at 0.8 pg/mL, it is observed that the diameter undergoes an increase of 1.7 times passing from a cast to 40 jets, exhibiting good repeatability; the mean intensity undergoes an increase of 15 times passing from a jet to 40 jets and this can always be justified with the accumulation effect.

These findings pave the way for new possible research:

- continue to investigate the accumulation effect in the case of the low volume range through further studies in combination with simulations;

- continue to investigate the behavior at intermediate concentrations, doing further tests with more repetitions.;
- continuing tests by performing replicates of the spots with always new load volume to investigate the improvement in intensity repeatability.

REFERENCES

- [1] Osmekhina, E.; Neubauer, A.; Klinzing, K.; Myllyharju, J.; Neubauer, P. Sandwich ELISA for quantitative detection of human collagen prolyl 4-hydroxylase. *Microb. Cell Factories* 2010, 9, 48. [CrossRef] [PubMed]
- [2] Leeming, D.J.; Sand, J.M.B.; Nielsen, M.J.; Genovese, F.; Martinez, F.J.; Hogaboam, C.M.; Han, M.K.; Klickstein, L.B.; Karsdal, M.A. Seriological Investigation of the Collagen Degradation Profile of Patients with Chronic Obstructive Pulmonary Disease or idiopathic Pulmonary Fibrosis. *Biomark. Insights* 2012, 7, 119-126
- [3] S. Itri, D. Del Giudice, M. Mugnano, V. Tkachenko, S. Uusitalo, A. Kokkonen, I. Pakkila, H. Ottevaere, Y. Nie, E. Mazzon, A. Gugliandolo, P. Ferraro, S. Grilli, A pin-based pyro-electrohydrodynamic jet sensor for tuning the accumulation of biomolecules down to sub-picogram level detection ()
- [4] R. Rega, M. Mugnano, E. Olandro, V. Tkachenko, D. del Giudice, G. Bagnato, P. Ferraro, S. Grilli and S. Gangemi, Detecting Collagen Molecules at Picogram Level through Electric Field-induced accumulation, *Sensors* 2020, 20, 3567
- [5] Gao, w.; Emaminejad, S.; Nyein, H.Y.Y.; Challa, S.; Chen, K.; Peck, A.; Fahad, H.M.; Ota, H.; Shiraki, H.; Kiriya, D.; et al. Fully integrated wearable sensor arrays for multiplexed in situ perspiration analysis. *Nature* 2016, 529, 509-514. [CrossRef] [PubMed]
- [6] Ray, T.R.; Choi, J.; Bandodkar, A.J.; Krishnan, S.; Gutruf, P.; Tian, L.; Ghaffari, R.; Rogers, J.A. Bio-integrated wearable systems: A comprehensive review. *Chem. Rev.* 2019, 5461-5533. [CrossRef] [PubMed]

- [7] Mujawar, M.A.; Gohel, H.; Bhardwaj, S.K.; Srinivasan, S.; Hickman, N.; Kaushik, A. N.; Kaushik, A. Nano-enabled biosensing system for intelligent healthcare: Towards COVID-19 management. *Mater. Today Chem.* 2020, *17*, 100307 [CrossRef] [PubMed]
- [8] V. Tkachenko, R. Schwödianer, R. Rega, S. Itri, M. Mugnano, D. del Giudice, H. Ottevaere, Y. Nie, P. Ferraro and S. Grilli, High-Rate Accumulation of Tiny Aqueous Droplets Using a Pyroelectrohydrodynamic Jet System, *Adv. Eng. Mater.* 2022, *24*, 2100756.
- [9] Tesi Sara Coppola
- [10] S. Grilli, L. Miccio, V. Vespini, A. Finizio, S. De Nicola, and P. Ferraro, Liquid micro-lens array activated by selective electrowetting on lithium niobate substrates, Vol. 16, Issue 11, pp. 8084-8093 (2008)
- [11] S. Grilli, V. Vespini, P. Ferraro, Surface-Charge Lithography for Direct PDMS Micro-Patterning, *Langmuir* 2008 Dec 2;24(23):13262-5
- [12] R. Rega, M. Mugnano, E. Oleandro, V. Tkachenko, D. del Giudice, G. Bagnato, P. Ferraro, S. and S. Gangemi, Detecting Collagen Molecules at Picogram Level through Electric Field-Induced Accumulation, *Sensors* 2020, *20*, 3567; doi:10.3390 /s20123567
- [13] P. Ferraro, S. Coppola, M. Paturzo and V. Vespini, Dispensing nano-pico droplets and liquid patterning by pyroelectrodynamic shooting, *Nature Nanotechnology* 5, 429(2010)
- [14] A. Puerto, S. Coppola, L. Miccio, V. Vespini, A. García-Cabañes, M. Carrascosa and P. Ferraro Droplet Ejection and Liquid Jetting by Visible Laser irradiation in pyro-photovoltaic Fe-doped LiNbO₃ platforms *Adv. Mater. Interfaces* 2021, *8*, 2101164

- [15] EM De Miguel, J. Limeres, M. Carrascosa, L. Arizmendi, *J. Opt. Soc. Sono. B* 2000, 17, 1140
- [16] N. Mkhize, H. Bhaskaran, Electrohydrodynamic Jet Printing: Introductory Concepts and Considerations, *Small Sci.* 2022, 2, 2100073
- [17] M. Mao, J. He, X. Li, B. Zhang, Q. Lei, Y. Liu, D. Li, *Micromachines* 2017, 8, 1.
- [18] S. Zargham, S. Bazgir, A. Tavakoli, A. Saied Rashidi, R. Damerchely, The Effect of Flow Rate on Morphology and Deposition Area of Electrospun Nylon 6 Nanofiber, *Journal of Engineered Fibers and Fabrics* Volume 7, Issue 4 – 2012
- [19] K. Sarkar, P. Hoos, A. Urias, Numerical Simulation of Formation and Distortion of Taylor Cones, *J. Nanotechnol. Eng. Med.* Nov 2012, 3(4): 041001
- [20] O. Gennari, L. Battista, B. Silva, S. Grilli, L. Miccio, V. Vespini, S. Coppola, P. Orlando, L. Aprin, P. Slangen and P. Ferraro, Investigation on cone jetting regimes of liquid droplets subjected to pyroelectric fields induced by laser blasts, *Appl. Phys. Lett.* 106, 054103 (2015)
- [21] V. Vespini, S. Coppola, M. Todino, M. Maturzo, V. Bianco, S. Grilli and P. Ferraro, Forward electrohydrodynamic inkjet printing of optical microlenses on microfluidic devices, *Lab Chip*, 2016, 16, 326-333
- [22] S. Grilli, L. Miccio, O. Gennari, V. Vespini, L. Battista, P. Orlando, P. Ferraro, Active accumulation of very diluted biomolecules by nano-dispensing for easy detection below the femtomolar range, *Nature communications* 5:5314

[23] Al-Shibaany, Z.Y.A.; Hedley, J.; Hu, Z. Micromachining lithium niobate for rapid prototyping of resonant biosensors. *IOP Conf. Ser. Mater. Sci. Eng.* 2014, 65, 012030. [Crossref]

[24] Al-Shibaany, Z.Y.A.; Penchev, P.; Hedley, J.; Dimov, S. Laser micromachining of lithium niobate-based resonant sensors towards medical devices applications. *Sensors* 2020, 20, 2206. [CrossRef]

[25]<http://d1zyp9ayga15t.cloudfront.net/CPmanual/MeasureImageIntensity.html#:~:text=Measure%20Image%20Intensity%20measures%20the,measurement%20to%20pixels%20within%20objects>

Marilina Mancini acknowledges the EU funding within the Horizon 2020 Program, under the FET-OPEN Project “SensApp”, Grant Agreement n.829104.

ACKNOWLEDGMENTS:

Thanks to Professor Pier Luca Maffettone for the immense availability.

Thanks to Simonetta and all the CNR team, for their constant help and for their great availability towards me.

Thanks to my parents for always encouraging me and for always supporting me, without them nothing would have been possible.

Thanks to my sister Rossana, to be always ready to listen to me and to have brought a breath of joy even in the most difficult moments.

Thanks to Giuseppe, to always be there, to support and endure me at all times and to always be ready to help me.

Thanks to Bruna, for having been the shoulder on which I cried in the dark times and for having enjoyed my achievements. You are my older sister.

Thanks to Antonella, lifelong friend with whom I really shared everything.

Thanks to Floriana, friend with whom I have shared anxieties for 15 years, it could not but happen that we shared the same week of graduation session.

How not to thank my favorite twins, we shared every single moment of this journey. In no time, you became friends. It wouldn't have been the same without you.

And finally, thanks to myself for never giving up.

